

PAPER • OPEN ACCESS

Advanced laser-driven ion sources and their applications in materials and nuclear science

To cite this article: M Passoni *et al* 2020 *Plasma Phys. Control. Fusion* **62** 014022

View the [article online](#) for updates and enhancements.



IOP | ebooks™

Bringing you innovative digital publishing with leading voices to create your essential collection of books in STEM research.

Start exploring the collection - download the first chapter of every title for free.

Advanced laser-driven ion sources and their applications in materials and nuclear science

M Passoni¹, F M Arioli, L Cialfi, D Dellasega², L Fedeli¹, A Formenti, A C Giovannelli, A Maffini, F Mirani, A Pazzaglia, A Tentori², D Vavassori, M Zavelani-Rossi and V Russo

Dipartimento di Energia, Politecnico di Milano, Milan, Italy

E-mail: matteo.passoni@polimi.it

Received 30 July 2019, revised 24 October 2019

Accepted for publication 12 November 2019

Published 6 December 2019



CrossMark

Abstract

The investigation of superintense laser-driven ion sources and their potential applications offers unique opportunities for multidisciplinary research. Plasma physics can be combined with materials and nuclear science, radiation detection and advanced laser technology, leading to novel research challenges of great fundamental and applicative interest. In this paper we present interesting and comprehensive results on nanostructured low density (near-critical) foam targets for TW and PW-class lasers, obtained in the framework of the European Research Council ENSURE project. Numerical simulations and experimental activities carried out at 100 s TW and PW-class laser facilities have shown that targets consisting of a solid foil coated with a nanostructured low-density (near-critical) foam can lead to an enhancement of the ion acceleration process. This stimulated a thorough numerical investigation of superintense laser-interaction with nanostructured near-critical plasmas. Thanks to a deep understanding of the foam growth process via the pulsed laser deposition technique and to the complementary capabilities of high-power impulse magnetron sputtering, advanced multi-layer targets based on near-critical films with carefully controlled properties (e.g. density gradients over few microns length scales) can now be manufactured, with applications outreaching the field of laser-driven ion acceleration. Additionally, comprehensive numerical and theoretical work has allowed the design of dedicated experiments and a realistic table-top apparatus for laser-driven materials irradiation, ion beam analysis and neutron generation, that exploit a double-layer target to reduce the requirements for the laser system.

Keywords: laser-plasma interaction, laser-driven ion acceleration, nanostructured materials, particle-in-cell, materials characterization, neutron generation, ion beam analysis

(Some figures may appear in colour only in the online journal)

¹ Now at Commissariat à l'énergie atomique et aux énergies alternatives (CEA), Gif-sur-Yvette, France.

² Now at Université de Bordeaux, Bordeaux, France.



Original content from this work may be used under the terms of the [Creative Commons Attribution 3.0 licence](https://creativecommons.org/licenses/by/3.0/). Any further distribution of this work must maintain attribution to the author(s) and the title of the work, journal citation and DOI.

1. Introduction

The interest for compact, flexible and versatile ion sources is increasing for many applications in a number of scientific, technological and societal applications ([1] and references therein). In this context laser-plasma based ion acceleration [2–4] represents a promising and interesting alternative to conventional accelerators, addressing some of their limitations

such as non-tunable energy, radioprotection issues, high costs, non-portable size.

The acceleration scheme is based on the interaction of an ultra-intense ultra-short laser pulse ($I > 10^{18} \text{ W cm}^{-2}$) with a target, which rapidly ionizes turning into a plasma. The coupling of the laser with the plasma induces a strong charge separation and, consequently, intense longitudinal electric fields which are responsible for the ion acceleration process. Several laser-based ion acceleration mechanisms have been proposed in the last two decades [5–7] among which one of the most studied and understood is the so-called target normal sheath acceleration (TNSA) [8, 9]. In this scheme, the laser irradiates a μm -thick solid target. The energy of the laser is partially absorbed by the electrons of the target, which expand at relativistic energies towards the back side, generating an intense sheath electric field (few $\text{MV } \mu\text{m}^{-1}$). This field drives the acceleration of the light ions located on the rear surface of the target. The result is the emission of a bunch of ions with a peculiar exponential energy spectrum and a well-defined cut-off energy, extending to the multiple-MeV range.

The great potential of laser-driven ion acceleration stimulates different research activities. From a fundamental point of view the main interest is the study of novel laser-plasma interaction regimes. A complementary, application-oriented approach aims to tailor the acceleration process for specific purposes. This intends to address several issues, such as operating at high repetition rates and ensuring the stability and the reliability of the ion beams.

Both aspects can naturally be related to an interest in the enhancement of the acceleration performances, in terms of maximum energy and/or number of accelerated ions. A widely investigated method relies on the continuous progress in laser technology, through the improvement of relevant laser parameters (pulse energy, power, intensity) along two possible directions: superhigh-power, multi-PW pulses [10, 11], with an energy of at least tens of J but with a low repetition rate (from one shot per 10 s seconds down to few shots per day), or less powerful laser pulses in the order of tens or hundreds of TW, with tens mJ-few J energy, operating at frequencies from Hz up to few kHz. This second laser concept is particularly interesting as it would allow realizing compact devices, working at high repetition rates, towards table-top accelerators [12, 13].

A complementary approach focuses on the control and optimization of the laser-plasma coupling, with the aim of allowing a more efficient laser absorption and, in turn, to enhance the number and cut-off energy of the accelerated ions. In this regard many efforts are made to conceive and engineer the irradiated targets, tailoring their properties for the specific interaction regime [14, 15].

In this frame, a large body of research confirms that the laser-plasma coupling is largely improved in the near-critical regime [16–20], i.e. when the plasma electron density is close to the critical value ($n_e \sim n_c = m_e \omega^2 / 4\pi e^2$, where ω is the laser frequency, and e and m_e are the charge and the electron mass), thanks to the volumetric interaction, the generation of energetic electrons and the efficient energy absorption.

Exploiting this interaction regime in laser-driven ion acceleration schemes is appealing. However, it requires several challenges to be addressed. Experimentally, producing near-critical plasmas is already an issue. For the typical wavelength of high intensity laser systems (0.8–1 μm), the near-critical density corresponds to a mass density of few mg cm^{-3} . Very few options are available [21–24]. One of these is represented by nanostructured low-density materials. However, ultra-intense laser interaction with nanostructured materials is still poorly understood. Moreover, considerable efforts are required to accurately model these scenarios in numerical simulations.

In the context of laser-driven ion acceleration, one appealing option is to exploit this interaction regime within the TNSA mechanism by using double-layer targets, where a near-critical layer is attached to the solid foil (in this paper we will refer to this kind of targets as DLTs), optimizing laser conversion to hot electrons and thus achieving an enhanced TNSA regime [25, 26].

An additional challenge to ensure the reproducibility of laser-driven ion sources and hence reliable operation at a high repetition rate is to achieve satisfactory control of the solid layer properties. One option is to move from conventional commercial foils, which can present some defectivity (see section 3.3 for more details), to the production of free-standing films with reliable and tailored properties.

Advances in laser technology and the development of an optimized DLT could lead to a compact, high-repetition rate laser-driven ion source. This source could be ideally suited for a number of applications in materials and nuclear science, like advanced material characterization [27], neutron generation [28, 29] and radioisotope production [30, 31].

The European project ENSURE (exploring the new science and engineering unveiled by ultraintense ultrashort radiation interaction with matter) [32], funded by the European Research Council (ERC), aims at facing and addressing all the above mentioned challenges.

In this article, we review our main achievements and present some of the most recent novel, unpublished, developments in all these research areas. The paper is organized as follows. In section 2 the theoretical investigation of the influence of realistic low-density nanostructured materials on the intense laser-plasma interaction in the near-critical regime is discussed. In section 3 we report the design and experimental production of double-layer targets and their exploitation in ion acceleration experimental campaigns. In section 4 the modelling of the enhanced TNSA regime is described. Finally, in section 5 we present the study of selected, promising and realistic applications in material and nuclear science which can benefit from this approach.

2. Physics of high-intensity laser interaction with nanostructured near-critical plasmas

The interaction between ultra-high intensity laser pulses and nanostructured materials is of great interest for numerous purposes, such as photon sources [33–38], charged particle

acceleration [18, 39–43] and studying ultra-high energy density physics [44, 45]. Nanostructured materials have complex density profiles with characteristic non-homogeneity on the nm– μm scale. For the laser-plasma interaction community, their allure mainly comes from their high versatility. Indeed, advanced materials synthesis techniques allow for a fine control of many properties of a nanostructure, such as its morphology, its size, the value of the characteristic scale-lengths, its average density and composition [22, 46]. This outstanding degree of flexibility gives access to a wide range of regimes of laser-plasma interaction [47, 48]. Another good reason why nanostructures are employed in experiments of high-intensity laser-plasma interaction is that they allow for a high conversion efficiency of laser energy into plasma kinetic energy. Most of the times this is due to the high surface-to-volume ratio and/or to the high degree of porosity which lets the laser propagate deep through matter, delivering most of its energy in it [44].

One could argue that a high-intensity laser pulse interacting with a nanostructured material not only readily turns it into a plasma, but also wipes out its nanostructure (also because of a possible prepulse). However, many ultra-intense lasers have a high temporal contrast ($>10^{10}$) on the few ps timescale [49, 50], so that the nanostructure might survive long enough to have an important effect during the interaction. However, we can estimate on physical grounds the timescale at which the nanostructure may be destroyed. Indeed, the expansion of a nanometric structure—say a nanoparticle of radius $R \sim 10\text{ nm}$ —is a combination of hydrodynamic expansion and Coulomb explosion [51]. The characteristic velocity of the former is the ion sound speed $c_s \sim \sqrt{\gamma Z T_e / m_i}$, where γ is the adiabatic index (equal to 5/3 for a monoatomic gas), Z is the ion atomic number, T_e is the electron temperature and m_i the ion mass. As for the latter, one can assume that all the electrons are ejected from the nanoparticle and then use the conservation of energy to calculate the characteristic velocity of a test ion initially in the nanoparticle, which is estimated to be of the order of $\omega_{pi} R$, where ω_{pi} is the ion plasma frequency. Considering reasonable parameters (i.e. $Z = 6$, $A = 12$, $T_e = 100\text{ keV}$, $n_e = 200n_c$), both characteristic velocities turn out to be of the order of $\sim 1\text{--}10\ \mu\text{m ps}^{-1}$. Assuming the gaps between the structures to be $\sim 1\ \mu\text{m}$, this means that the nanostructure could be washed away in a time of the order of 100 fs. Therefore, studying the interaction in that time-scale, which is comparable with most high-intensity lasers duration, is interesting, also because some reminiscence of the nanostructure may survive on longer time-scales.

At present day, a key issue from the theoretical/numerical standpoint is to provide an accurate modeling of the laser, the nanostructured material and their interaction. To address this point, we designed and performed multi-dimensional (2D and 3D) particle-in-cell (PIC) simulations [52] of superintense laser-plasma interaction where we considered the plasma nanostructure, with the main goal to assess its role in the interaction process [53]. We did this by comparing the behavior of the nanostructured plasmas with homogeneous plasmas having the same average density. In this section, we

highlight the main results of these simulation campaigns [19, 20], providing the general picture and rationale under which our work was carried out, and add further insights. All simulations were performed with the massively parallel, open source PIC code *Piccante* [54].

By means of 2D simulations, we explored a wide range of laser intensities ($a_0 = eA_0/m_e c^2$, with A_0 the laser peak vector potential) and initial average electron densities (n_0) (see figure 1(a)). In all the simulations the laser is Gaussian in the transverse plane with $5\ \lambda$ waist and has \cos^2 longitudinal profile with a full-width-half-maximum of the field equal to $15\ \lambda/c$. The interaction happens at normal incidence and linear P-polarization. In 2D the nanostructure was modeled as a collection of overdense nanospheres (radius = $0.05\ \lambda$, $Z/A = 1/2$, electron density = $90n_c$) randomly arranged in space. On the other hand, by means of 3D simulations, we explored a selected region of the parameter space (a_0, n_0), this time employing realistic morphologies, which are inherently of three-dimensional nature. Figure 1(a) shows how we explored the parameter space (a_0, n_0 , dimensionality) in these simulation campaigns, while figure 1(b) shows the different morphologies used in the 3D simulations: homogeneous, foam-like, ordered nanowires and random nanowires plasmas (see [18] and section 3 for further details). All simulated plasmas are chosen to be long enough so that the laser can be completely absorbed in them at least in the lowest intensity cases. Note from figure 1(a) that we decided to keep the following parameter (an effective ‘transparency parameter’ which takes into account relativistic effects [55–57])

$$\bar{n} = \frac{n_0/n_c}{\sqrt{1 + a_0^2/2}} \quad (1)$$

constant in some subsets of 2D simulations (each represented by one of the colored ‘diagonals’ in figure 1(a)). The larger \bar{n} the more opaque the plasma is to the laser pulse. In this way we could clearly identify three qualitatively different regimes of interaction: one where the laser is able to propagate through the plasma and be completely absorbed in it (‘relativistically transparent diagonal’ in figure 1(a)), one closer to the transparency threshold (‘relativistically near-opaque diagonal’ in figure 1(a)) and an intermediate one.

We found out that in the ‘relativistically near-opaque diagonal’ the main role of the nanostructure is that of greatly (\sim four-fold) enhancing the laser energy absorption by the plasma populations (see figure 1(c)).

Such enhancement is due to a corresponding enhancement of energy absorption of both electrons (from $\sim 35\%$ to $\sim 60\%$ in 2D, from 20% to 60% in 3D) and ions (from few% to $\sim 50\%$ in 2D, from few% to $\sim 20\%$ in 3D). The nanostructure has a striking effect on ion absorption in this regime: while ions essentially remain cold with homogeneous plasmas, they are able to absorb a significant fraction of energy in presence of a nanostructure. Indeed, with a nanostructure, ions gain energy from the local electric fields that set up as a consequence of a Coulomb-like explosion of the nanoparticles, a process that is completely absent in a homogeneous plasma.

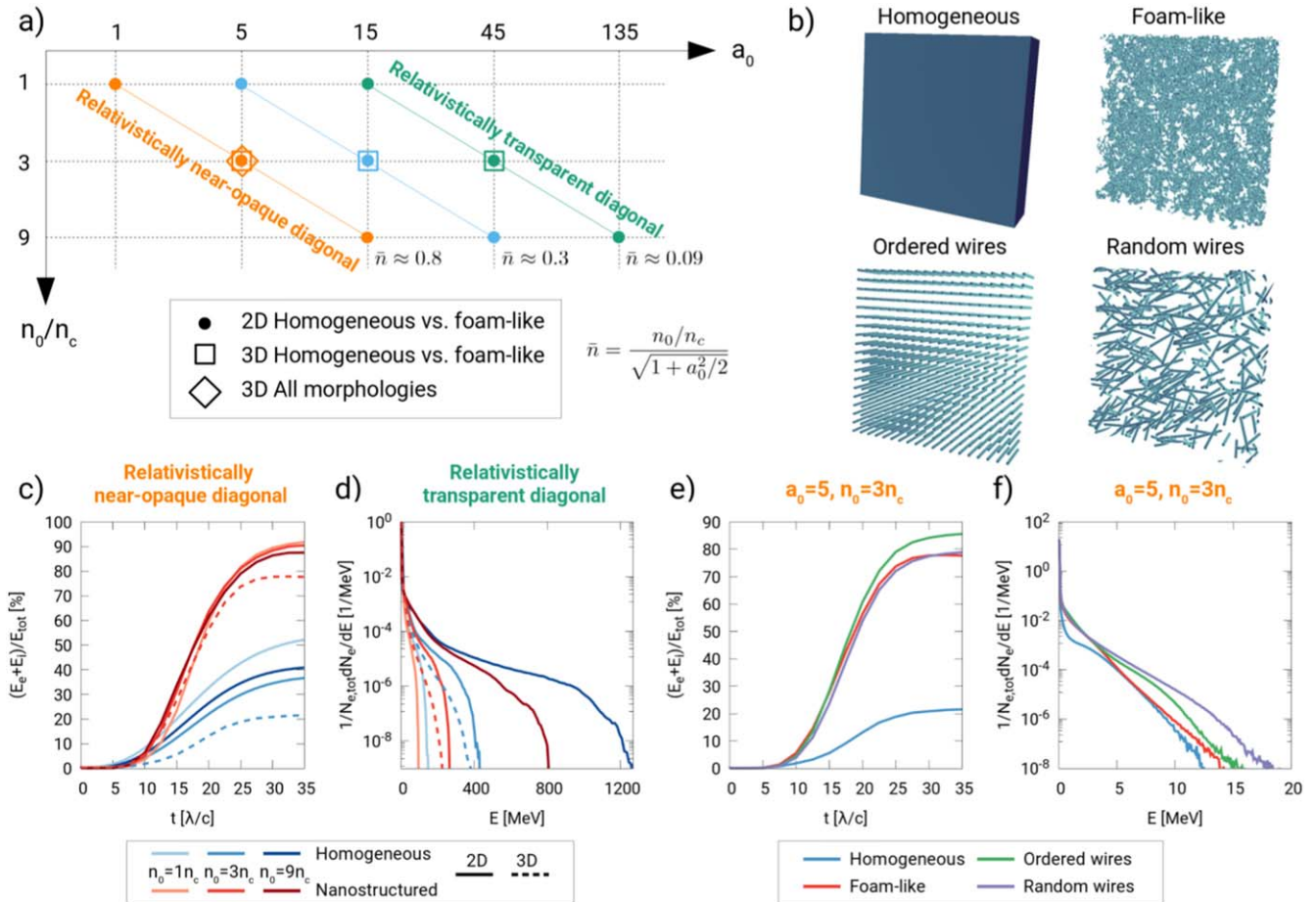


Figure 1. (a) Parameter space given by the laser intensity (a_0) and the initial average electron density (n_0/n_c) explored in the 2D (dots) and 3D (squares) PIC simulation campaigns. The subsets of simulations belonging to the three colored diagonals have the same value of the ‘transparency parameter’ \bar{n} , equal to 0.8 (orange, ‘relativistically near-opaque diagonal’), 0.3 (blue) and 0.09 (green, ‘relativistically transparent diagonal’). (b) Plasma morphologies simulated with 3D PIC simulations: homogeneous, foam-like, ordered wires and random wires. The images qualitatively represent the plasma electron density as initialized in the PIC code. (c), (e) Fraction of the total energy (E_{tot}) that is kinetic plasma energy (of both electrons and ions, $E_e + E_i$) as a function of time (t). Note that E_{tot} is approximately the laser energy E_L , since at the initial time the plasma energy $E_e + E_i$ is negligible with respect to E_L . Therefore, this quantity can be also interpreted as the plasma absorption of laser energy in time. (d), (f) Electron spectra for the simulations in the transparent diagonal. All spectra (dN_e/dE) are normalized to their area ($N_{e,tot}$). (c) and (d) panels refer to the simulations in the opaque diagonal, showing a comparison between homogeneous (blue) and nanostructured (red) plasmas in 2D (solid lines) and 3D (dashed lines). In 2D the nanostructured plasma is a collection of random nanospheres, while in 3D is the foam-like plasma. (e) and (f) panels refer to the 3D simulations with $a_0 = 5$ and $n_0 = 3n_c$ (opaque diagonal), performed for all the plasmas morphologies shown in panel (b).

On the other hand, in the ‘relativistically transparent diagonal’, the plasmas are transparent enough to the laser to have a similar electron absorption rate in every case ($\sim 70\%$ in 2D, $\sim 40\%$ in 3D). A higher ion absorption with the nanostructure is observed in this case too (from few% with homogeneous plasmas both in 2D and 3D to 5% in 2D and 10% in 3D with nanostructured plasmas), even if to a much milder extent than in the ‘relativistically near-opaque diagonal’. Here, the main role of the nanostructure is that of reducing the maximum electron energies (see figure 1(d)). The highest energy electrons are accelerated by a direct laser acceleration [58] process, which is a resonant mechanism. With a nanostructure, this process is less efficient because of the irregular and disordered features, which fall back on the propagation of the laser field.

As for both these aspects, note that we observe a similar behavior with 3D simulations, when we compare homogeneous plasmas with foam-like plasmas (see figures 1(c) and (d), dashed lines). This somewhat validates the use of 2D simulations, as long as it is aimed at getting general trends and qualitative insights.

Lastly, we picked the case $a_0 = 5$ and $n_0 = 3n_c$ to be simulated with all the morphologies shown in figure 1(b). We chose the low intensity case, for two main reasons. First, being lower the intensity, the nanostructure would survive longer and so a more important effect on the interaction process should be expected. Second, a normalized amplitude $a_0 = 5$ can be provided by few 10 s TW laser systems [59], which can be very compact [60]. Therefore, this regime is relevant for the development of compact, table-top ion

sources and their applications (see section 5). We observe that, regardless of the morphology, all plasmas absorb, at the end of the interaction, $\sim 80\%$ of the laser energy, to be compared with the $\sim 20\%$ absorption of the homogeneous plasma (see figure 1(e)). However, the details of the nanostructure deeply affect the absolute number of electrons accelerated at relativistic energies (>0.511 MeV), as seen in figure 1(f) and of the energy-angle distributions of both electrons and ions (not shown) [19].

The main outcome of these investigations is that the nanostructure and its morphology appear to have a significant impact on the interaction. Not including their description could lead to a misinterpretation of the data, which, besides, would strongly depend on the specific regime of interaction.

These results give insights on the role played by a nanostructure upon the interaction with a superintense laser pulse. In any case, understanding how this reflects on the ion acceleration process in a TNSA-like picture needs dedicated investigations. We will explore more in depth this other scenario focusing on compact laser systems in section 5.1. According to the results presented in this section, we expect the role of the nanostructure in TNSA to strongly depend on the regime of interaction.

In the following section, we rely on these very results to explore more in depth the features of DLTs and their design/production for laser-driven ion acceleration experiments.

3. Foam-based double-layer targets for enhanced laser-plasma ion acceleration

In the context of laser-driven ion acceleration, a strategy to enhance the TNSA regime can rely on the exploitation of DLTs, where a near-critical layer is attached to a solid foil [17, 25]. Both theoretical investigation about laser coupling with nanostructured near-critical plasma (see section 2) and experimental campaigns in different configurations (see section 3.2) [18, 26, 40, 41] have shown that this kind of targets is able to significantly increase both the energy and number of accelerated ions. Here we discuss our more recent improvements in the framework of the production and characterization of near-critical nanostructured materials.

In addition, we review the principal results obtained during an experimental laser-ion acceleration campaign aiming to test the performances of the DLT concept.

Finally, we describe our approach to develop advanced DLTs for laser-driven ion acceleration, combining techniques for the production of the entire target on a suitable holder, with controlled properties at different scales, from cm to nm.

3.1. Production and characterization of nanostructured carbon foams

The vast majority of the laser systems considered for laser-driven ion acceleration exploits near-infrared wavelengths ($\lambda \approx 800$ nm for Ti:Shapphire, $\lambda \approx 1060$ nm for Nd:Glass), resulting in a critical electron density of the order of 10^{21} electrons/cm³. For most materials, the corresponding mass

density is about $5\text{--}10$ mg cm⁻³, roughly two or three orders of magnitude less than the typical density of a solid.

One can devise very few options to achieve a solid-state material with such a low mass density; the most studied is represented by nanostructured materials with a very high void fraction ($\geq 99\%$), such as aerogels, nanowire bundles, carbon nanotubes foams and nanofoams [18, 22, 39, 47, 61].

In previous works, we have shown that ns Pulsed Laser Deposition (ns-PLD) [62], which exploits pulses with ns duration, 100 s mJ energy pulses and 10 Hz repetition rate, is a versatile tool to produce carbon nanofoams suitable as near-critical layer in targets for laser-driven ion acceleration [21, 26, 40, 41].

Here we review the most recent advances related to the design/production of nanofoam materials for laser-driven ion acceleration. The focus was on two main objectives: the development of an advanced tool for the characterization of nanofoam density on different scale-length and a better understanding of the foam growth that could allow detailed control of the foam nanostructure. The obtained results allowed to extend the space of achievable material properties, especially in terms of density and homogeneity scale. In addition, we also present here our novel results about production of nanofoams in the new regime we are exploring, called fs-PLD.

Concerning the first goal, we have proposed a novel scheme to exploit the Energy Dispersive x-ray Spectroscopy (EDXS) technique to retrieve information about the nanofoam density [63].

The technique exploits a theoretical modeling of both electron transport in the nanofoam/substrate system and characteristic x-ray emission. Differently to previous similar approaches [64], this method does not require a reference sample, since only the x-ray intensities of carbon (relative to the nanofoam) and substrate material are needed.

In addition to a higher measurement simplicity and improved accuracy, our method also allows to retrieve detailed density and composition maps (see figure 2(b)) with a lateral resolution ~ 200 nm and for sample density below 5 mg cm⁻³. These features are especially valuable for the characterization of foam-based targets for laser-driven ion acceleration, since the non-uniformity of the near-critical layer at a scale length comparable with laser spot size can significantly affect the laser-plasma interaction.

In parallel, we have developed a novel theoretical framework to describe the process of nanofoam growth in PLD experiments [65]. In particular, we have proposed a 'snow-fall-like' model that explains the peculiar nanofoam morphology as the result of the superposition and coalescence of micrometer-sized aggregates of carbon nanoparticles (NPs). We demonstrated that the aggregation process occurs in flight, i.e. before the aggregate landing, and that the aggregation time scale is dominated by the time elapsed by two subsequent laser shots. As a consequence, the average aggregate size depends on the repetition rate of the laser with a negative exponent power law.

This feature provides a novel -and largely unexplored- degree of freedom in PLD experiments, which can be exploited to tailor the nanofoam properties (e.g. density and

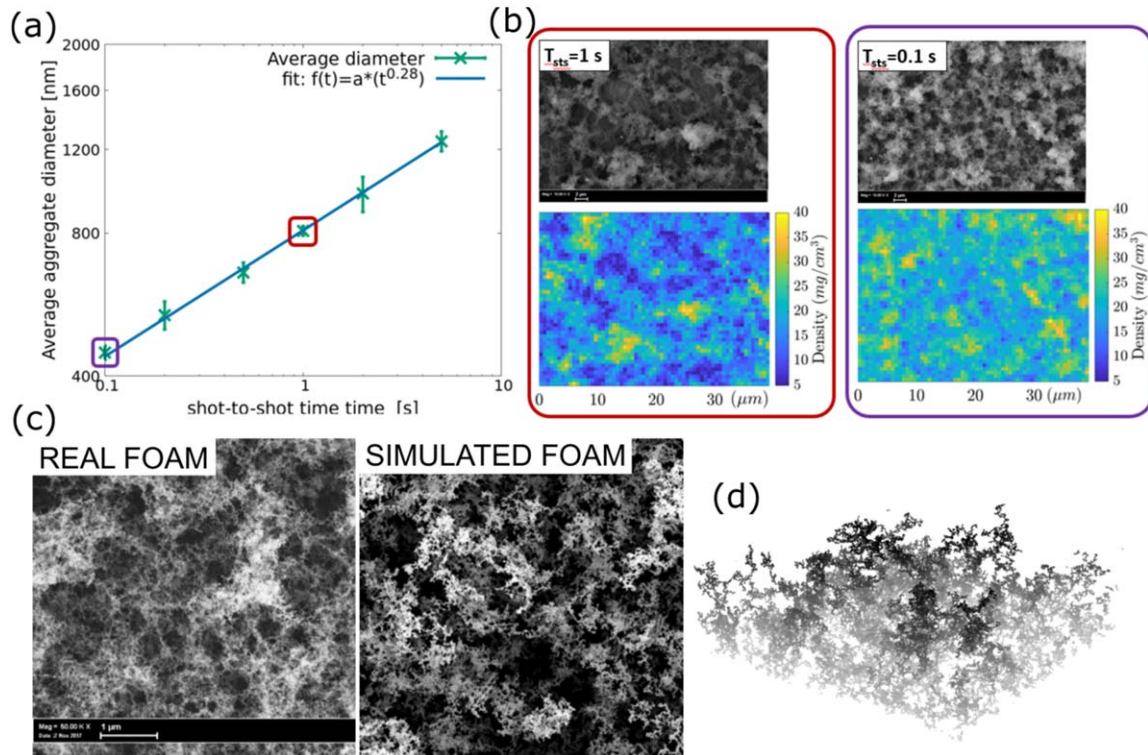


Figure 2. (a) Shows the average aggregates diameter, green crosses, generated by the ns-PLD (10 shots, 700 Pa of Argon as background gas, 1.7 J cm^{-2} fluence) as a function of the shot-to-shot time (the inverse of the laser repetition rate). The continuous blue curve represents a power law fit. Figure (b) shows on the top the SEM images of nanofoams generated by ns-PLD with the parameter of figure (a), with two different values of the laser repetition rate: on the left 1 Hz, on the right 10 Hz. On the bottom the density map (obtained with the EDXS method), relative to the SEM images, are represented. Figure (c) shows the comparison of a real SEM image of a nanofoam and the simulated SEM image of a ‘numerical’ nanofoam, generated with the DLCCA algorithm. Figure (d) shows a three-dimensional view of a DLCCA nanofoam.

uniformity) down to the nanoscale. This is highlighted in figure 2(a), using data from [65].

The insights gained through the deep understanding of the growth dynamics described above have opened new perspectives in the development of numerical algorithms to simulate the foam morphology in terms of rigid spheres arranged in a fractal-like structure. One approach is the diffusion-limited aggregation (DLA) process [66], where primary particles walk randomly due to Brownian motion and cluster together to form the aggregate. Therefore, the simulated structure is obtained with a single-step algorithm.

On the contrary, here we decided to use a two-step algorithm to implement a diffusion limited cluster-cluster aggregation (DLCCA) process [67]. The first step describes the NP aggregation with a Monte-Carlo method, where N hard spheres are free to move randomly in three dimensions until they collide and irreversibly stick together. Once all the NPs are merged in a single aggregate, the latter is deposited toward the substrate with a ballistic trajectory and a rigid body motion; it can stick either to the substrate or to another previously landed aggregate (second step). These steps are repeated until a ‘numerical foam’ of a certain desired thickness is grown.

As can be appreciated by the comparison in figure 2(c), the resulting ‘numerical foam’ is very similar to the morphology of a real ns-PLD nanofoam as seen in SEM

images, thus giving another indication that the proposed snowfall model offers a meaningful description of nanofoam growth dynamics. We also point out that the DLCCA structure, represented in figure 2(d), can be profitably used to describe realistically the ‘foam-like’ plasma shape in 3D PIC simulations, as discussed in section 2 and further in section 5.1.

This outcome allowed us to show that the main nanofoam properties depend on the NPs dimension r_{np} and the aggregate radius R , which in turn depends on N with a fractal scaling $N = (R/r_{np})^{d_f}$, where d_f is the fractal dimension. In ns-PLD regime it is difficult to achieve an independent control over those quantities, mainly because the main parameters of the process (i.e. laser fluence and background gas pressure) invariably affect both the NP synthesis (and thus N and r_{np}) and NP aggregation (related to R and d_f).

To overcome this limitation, we have developed a new experimental set up at Politecnico di Milano and began to explore the PLD regime, called fs-PLD in the following, which exploits high peak power femtosecond pulses (<100 fs pulse width and 5mJ energy) at high repetition rate (1 kHz), from a Ti:Shapphire amplified laser system (Coherent, Astrella-V). This interaction regime is characterized by a high material removal efficiency, which may avoid the emergence of large particles, and by a repetition rate high enough to inhibit the adjustment of the NPs on the substrate [68]. It is

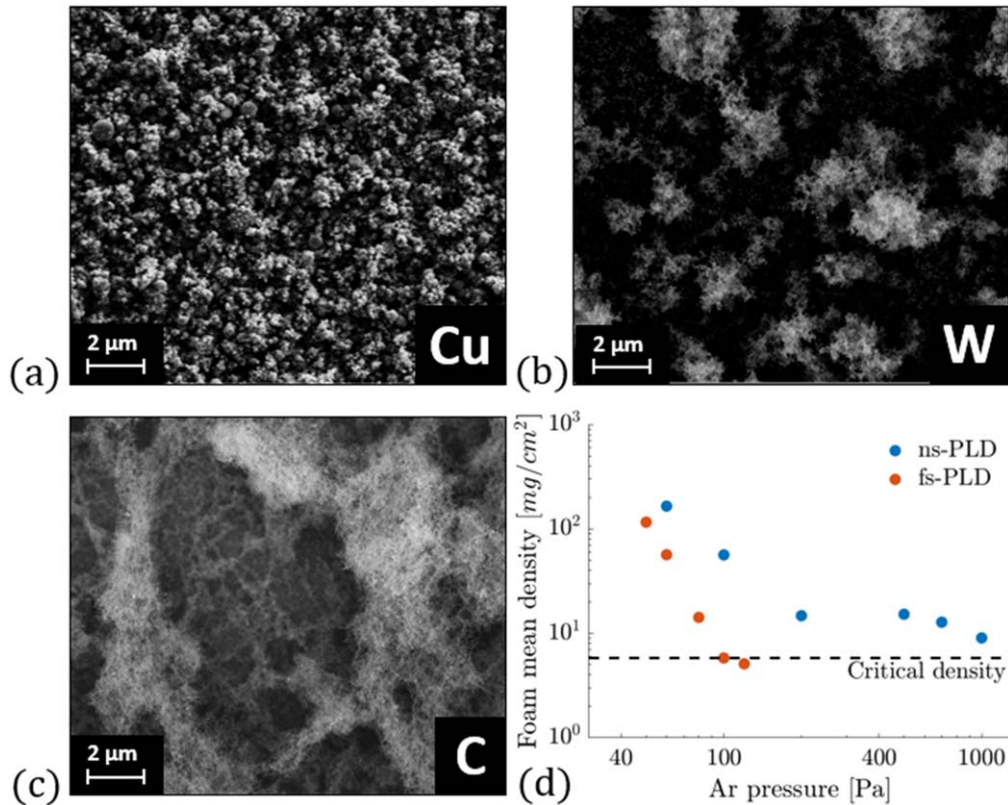


Figure 3. (a)–(c) Nanofoams produced by fs-PLD from different elements are shown. The ablated target was respectively copper, tungsten and carbon; the pulse energy was 5 mJ in all the cases; the pulse intensity on target was respectively $1.8 \times 10^{12} \text{ W cm}^{-2}$, $1 \times 10^{12} \text{ W cm}^{-2}$ and $1 \times 10^{12} \text{ W cm}^{-2}$; the ambient gas was argon with pressure equal to 100, 500 and 100 Pa. Figure (d) shows the C nanofoam mean density, calculated by the EDXS method, as a function of the argon background gas pressure. The blue dots refer to the nanofoam produced by the ns-PLD, while the orange dots refer to the fs-PLD; the dashed line marks the threshold of the carbon critical density at the laser wavelength of a Ti:Sapphire laser (800 nm).

also important to note that the NP synthesis occurs as a direct result of laser-target interaction and it is not necessarily mediated by the background atmosphere. This feature can be exploited to decouple the NPs synthesis and their aggregation, with a clear possible advantage in terms of fine control over material properties.

In particular this fs-PLD capability is used to produce nanofoams from different elements, as shown in figures 3(a)–(c), in which copper, tungsten and carbon foams are respectively shown. C nanofoams show the more porous structure, while the lower porosity is presented by Cu nanofoams and W nanofoams is an intermediate case. It should be pointed out that the material structure is not a function of the composition only, but it depends on several variables: among them, the ambient gas pressure and the pulse intensity on target play important roles. For example, figure 3(d) reports the C nanofoam average density as a function of the argon background pressure, clearly showing that a higher gas pressure results in a more porous structure. Conversely, it follows from the case of figure 3(a) that a higher laser intensity on target causes a lower confinement of the ablated NPs and a reduced porosity.

We finally remark that the efficient production of NPs in the fs-PLD allows the production of foams characterized by a lower density, compared to the ns-PLD case; this point is particularly interesting for the laser-driven ion acceleration,

since C nanofoams with density under n_c can be readily produced.

3.2. Laser-driven ion acceleration experiments with DLT

An experimental campaign aiming at testing the performances of the DLT concept was performed at the Center for Relativistic Laser Science (CoReLS), Institute for Basic Science (IBS) in Republic of Korea [40, 41, 69].

The used DLTs were composed by a commercial $0.75 \mu\text{m}$ -thick Al foil and a near-critical carbon foam layer deposited on it (about 7 mg cm^{-3} , corresponding to an electron density of $1.2 n_c$ when fully ionized), with foam thickness varying from $8 \mu\text{m}$ to $36 \mu\text{m}$. Bare $0.75 \mu\text{m}$ -thick solid Al foils (ST) were used as a reference. To investigate the role played by the Al substrate thickness a $1.5 \mu\text{m}$ -thick Al foil is also used, both bare and with a $12 \mu\text{m}$ foam. In the experiments, a 30-fs, PW-class Ti:sapphire laser was exploited. The pulse energy was 7.4 J on target (at full power), with a focal spot of $5 \mu\text{m}$ containing 22% of the total pulse energy in the FWHM area. Thus, the available intensity was about $4.5 \times 10^{20} \text{ W cm}^{-2}$. The targets were irradiated with a fixed incidence angle of 30° varying among P-, S-, and circular (C-) polarization. Thomson parabola spectrometers were used to measure the energy spectra of emitted ions.

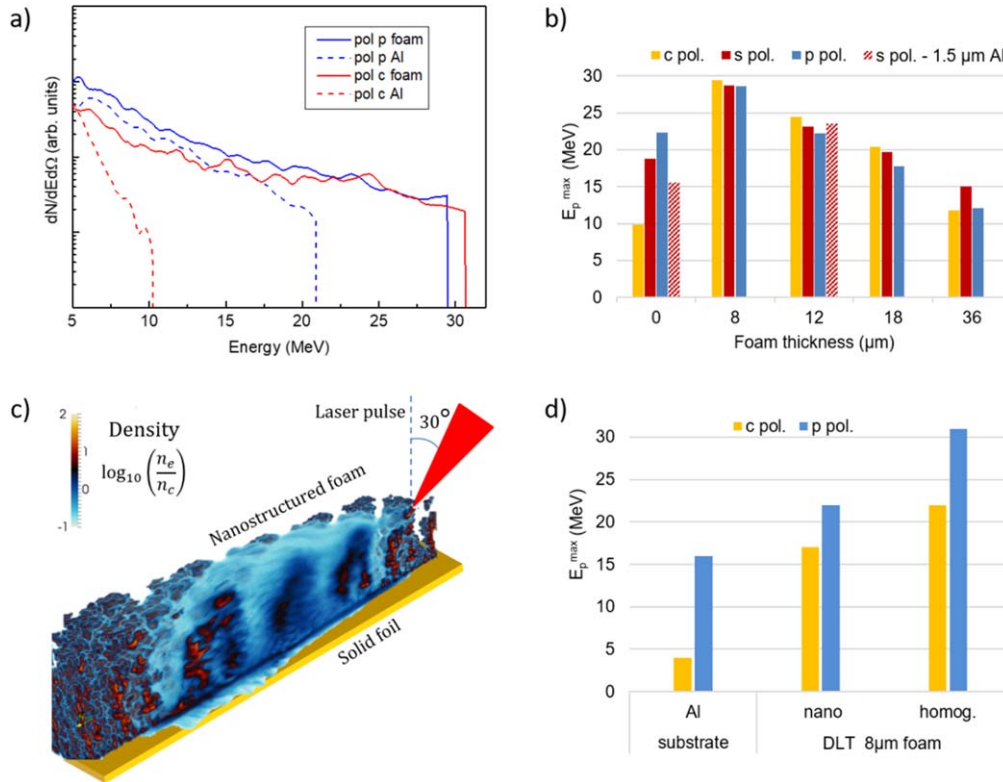


Figure 4. (a) TPS proton spectra of ST and DLT 8 μm thick considering different polarizations, P- (in blue) and C- (in red); (b) Maximum proton energy at different laser polarizations varying foam thickness; red-white dashed columns refers to 1.5 μm Al solid foil, bare and with 12 μm foam. (c) 3D-PIC simulations of the interaction between the fs laser pulse and a DLT composed by a solid foil and a nanostructured foam. The red cone represents the incident laser; (d) simulated maximum proton energy from Al foil, DLT with nanostructured and homogeneous foam, using P- and C- polarized laser pulses.

Figure 4(a) reports the experimental proton energy spectra relative to two different polarizations for the case of DLT with 8 μm foam compared with ST. All the spectra exhibit the characteristic trend of TNSA acceleration mechanism. For both polarizations a significant increase of the maximum proton energy (E_p^{\max}) is recorded when moving from ST to DLT. It is possible to define gain factors for the relevant experimental quantities as the ratio between the two values obtained using DLT and ST, respectively. Here we focus on E_p^{\max} (energy gain factor) and on the total number of protons with energy higher than a conventional value of 8 MeV (p number gain factor). With P-polarization we found an energy gain factor of about 1.4, going from 22 MeV for ST to 30 MeV for DLT, and a p number gain factor of 2. With C-polarization we found $E_p^{\max} = 10$ MeV with ST, lower with respect to the previous case, while $E_p^{\max} = 30$ MeV again using DLT. In this case the energy gain factor is about 3, while the p number gain factor is more than 20.

The effect of the laser polarization was investigated considering also S-polarization. The results are reported in figure 4(b) in terms of E_p^{\max} , distinguishing among different foam thicknesses. The observed values for E_p^{\max} with STs for P-, S- and C-polarization were 22, 18 and 10 MeV, respectively. This strong dependence on the polarization is due to different laser absorption efficiency in solid targets, well-known in the literature (see [2] and refs therein). On the

contrary, for DLTs E_p^{\max} is not affected by the polarization. This is ascribable to the different interaction mechanism in the foam with respect to solid foil as described in sections 2 and 5.1.

The results also show that E_p^{\max} is strongly influenced by the foam thickness, decreasing when a foam thickness greater than 8 μm is used. We observe that for DLT with 12 μm foam E_p^{\max} is comparable with the ST case, while an inversion is found considering 18 and 36 μm thick foams, where we found a lower E_p^{\max} than the ST case. This monotonic trend suggests that the optimal foam thickness should be ≤ 8 μm for the laser parameters adopted in this experiment.

We also studied the effect of the Al foil, using 0.75 and 1.5 μm thick Al foils for both STs and DLTs with near-critical foam. For STs a strong dependence of the acceleration performances on the Al thickness was observed; the use of thicker foils results in a lower E_p^{\max} of about 20%–30%. In contrast, no systematic difference in E_p^{\max} was observed for DLTs between the case of 0.75 and 1.5 μm Al foils (reported in figure 4(b) for the DLT with 12 μm foam).

We performed 3D PIC simulations to support the interpretation of the experimental data outlined here. The PIC code *Piccante* is used, modelling the ST with a bare 0.8 μm Al substrate ($n_e \cong 40n_c$) and the DLT with the same Al foil and a 8 μm foam. The foam was simulated either as a homogeneous near-critical layer or as a more realistic nanostructured foam,

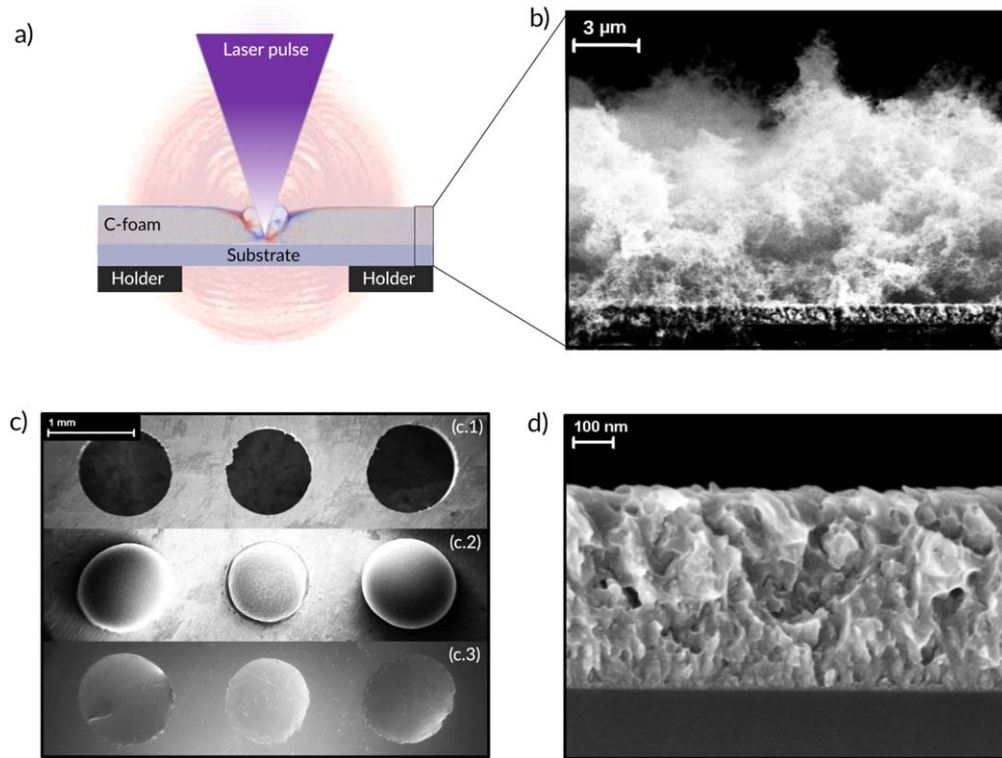


Figure 5. (a) Double layer target (DLT) conceptual scheme. (b) DLT SEM cross section view. (c) The top view of the holes of the holder at three steps. (c.1) Before filling the holes with sucrose. (c.2) After the sucrose solidification. (c.3) After the substrate deposition with HiPIMS. (d) SEM cross section view of the substrate.

designed using DLA approach (mentioned in section 3.1) [66], imposing in both cases $n_e \cong 1n_c$. The chosen laser parameters were: 30° incidence angle as in the experiment, P- and C- polarizations, intensity parameter $a_0 = 18$, beam waist $4 \mu\text{m}$ and pulse duration 31 fs. In figure 4(c) a scheme of the simulations is reported. The simulations show that the laser propagates through the entire nanostructured layer, as qualitatively reported in figure. During the interaction, volumetric heating occurs and the pulse is strongly absorbed by the foam electrons. Ion acceleration is due to an enhanced TNSA process (see also sections 4 and 5.1). E_p^{max} is reported in figure 4(d) for the three cases of ST, DLT with nanostructured foam and DLT with homogeneous foam, for C- and P-polarizations. Using DLTs, with either the homogeneous near-critical layer or the nanostructured foam, we observed an increase in E_p^{max} with respect to the bare Al target for both investigated polarizations, confirming the experimental trend. We also observe that, considering P-polarization, the DLTs with foams simulated as homogeneous layers lead to an overestimation of the experimental energy gain factor (1.9 versus 1.4), while the nanostructured foams match the experimental findings more closely (1.3 versus 1.4). In addition, we notice that the simulations of the foam as uniform layers show a strong polarization dependence of the ion spectra while the presence of a nanostructured foam strongly reduces the differences between the two investigated polarizations, as observed in the experiment.

3.3. Solid films production for advanced DLTs

In order to make laser-driven ion sources based on enhanced TNSA with DLT attractive for multiple applications [1, 29, 31], the DLTs properties must be finely controlled, in terms of both the near-critical and the solid layer, as well as with respect to their cohesion and overall integrity.

Within the framework of the ENSURE project, we propose a strategy to produce the whole DLT, directly on standardized perforated target holders. A scheme of the DLT is reported in figure 5(a), together with the SEM images of the developed system (figure 5(b)).

Regarding the near-critical layer, as described in section 3.1, ns-PLD and fs-PLD allow foams of different materials to be produced in wide ranges of thicknesses and densities down to the critical density.

Considering solid substrates in TNSA experiments, rolled commercial sheets with nominal thickness spanning between 100 s of nanometers and several microns are commonly employed [14]. These foils are usually metallic and available in a limited number of thicknesses and materials. Moreover, for sub-micrometric sheets, the thickness can be affected by a margin of error of $\pm 30\%$ with respect to the nominal value, as commonly reported by manufacturers. They can be also characterized by the presence of defects like pinholes and ripples. Finally, the foils are manually fixed or clamped on the perforated target holders with the risk of breakage, formation of wrinkles and ripples.

All these sources of uncertainty can strongly affect the shot-to-shot reproducibility of laser-driven ion sources. They also represent an obstacle to the realization of targets suitable for high repetition rate operation and the generation of a quasi-continuous beam.

The production of free-standing films is a viable route to overcome many of the aforementioned limitations. Some attempts recently appeared in literature. In particular, Micro-Electro-Mechanical System (MEMS) techniques have been used for nanometric scale DLC films fabrication [70]. For metallic sub-micrometric substrates production, Direct Current Magnetron Sputtering (DCMS) deposition on a sacrificial layer has been exploited [71].

In the procedure proposed here, the metallic films are directly deposited on the target holders via Magnetron Sputtering techniques. Beside the already mentioned fs-PLD, a Magnetron Sputtering facility has also been set up at Politecnico di Milano. This machine allows depositing metallic films both in Direct Current (DCMS) [72] and High Power Impulse Magnetron Sputtering (HiPIMS) [73] mode. These modes allow depositing films from few nanometers up to several micrometers of thickness and to tune the main properties (i.e. density, morphology, and stoichiometry). Both DCMS and HiPIMS rely on the application of a voltage between a cathode and an anode. The applied voltage triggers the formation of a plasma composed by electrons and ions from the background gas. By applying a magnetic field, the plasma is confined on the cathode surface. The gas ions sputter atoms from the cathode, which are subsequently deposited onto a support plate where the film grows. With DCMS the applied voltage is constant in time and the sputtered species are neutral.

On the contrary, with HiPIMS the power is periodically provided in short and much more intense impulses, leading to the formation of a denser plasma and to the deposition of energetic ions.

In general, DCMS films [74] deposited at room temperature are characterized by a columnar morphology, while HiPIMS films exhibit a more compact structure [75].

Our procedure to produce DLTs [76] starts with the deposition of a drop of sucrose solution in the holes of standardized holders (see figure 5(c.1)). Sucrose is a good compromise between different requirements: high solubility in water, fast solidification and low viscosity in solution.

The solution solidifies, resulting in the formation of a continuous surface (see figure 5(c.2)). Then, by suitably exploiting DCMS and HiPIMS depositions, a metallic film of titanium is grown on the sucrose layer. After the deposition, the sucrose layer is removed via dissolution in water in order to obtain the free-standing metallic substrate (see figure 5(c.3)). We chose titanium among others, since it is a common substrate material in laser-driven ion acceleration experiments [77]. Moreover, titanium is characterized by good mechanical and thermal properties. The Ti layer is grown alternating DCMS and HiPIMS depositions in order to better control its morphology, density and stress state. As a result, compact, quasi-amorphous substrates with thicknesses ranging from 300 nm up to 1 μm have been produced (see

figure 5(d)). The maximum measured thickness uncertainty is equal to $\pm 5\%$ over a substrate area of several cm^2 . The substrate density ranges between $\approx 80\%$ and 90% of the bulk value. More details about the properties of the deposited material will be reported in a dedicated, material science work.

Finally, after the foam deposition with the PLD technique, the final result is a double layer target (see figure 5(b)) whose most relevant properties can be controlled and optimized in order to enhance the TNSA process for given laser parameters.

4. Enhanced TNSA modeling

The theoretical description of the TNSA acceleration process, besides being of fundamental interest for a deeper understanding of the physical phenomenon, represents a crucial step for the selection of suitable experimental parameters and the design of advanced targets. In this section we describe our activities in this area in a wide range of experimental conditions obtained by an integrated analytical-numerical approach.

Several models to describe the TNSA process have been proposed in the literature; among them, the quasi-static Passoni-Lontano model aims at taking into account kinetic and relativistic effects in a self-consistent way [8, 78, 79].

This approach assumes that, following the laser pulse absorption, the population of electrons heated by the laser pulse reaches a stationary state which lasts for a time of the order of hundreds of fs. During this time, both the ions of the target bulk and the light ions of the contaminant layer, i.e. the ions on the rear target surface that are accelerated by the TNSA field, can be considered immobile because of their inertia. The stationary state reached by the hot electron population is described by a distribution function $f(x, p)$, which depends on the spatial variable x through the electrostatic potential $\varphi(x)$. The potential is in turn generated by the charge displacement itself, which can be self-consistently calculated by integrating $f(x, p)$ over the momenta of the bound electrons (i.e., those having negative total energy). This strongly non-linear system can be solved through numerical integration, yielding an estimation for the ion cut-off energy E_p^{max} as the potential energy experienced by a test particle of charge Ze placed at the rear surface of the target, namely $E_p^{\text{max}} = Ze\varphi(x=0) = Ze\varphi^0$.

As detailed in [8, 78, 79], the quasi-static model allows one to calculate the ion cut-off energy and the electrostatic field profile once the functional form of $f(x, p)$ and the maximum value of the potential (φ^*) are given.

If collisions can be neglected -as it should be expected for a relativistic plasma- the stationary state distribution function $f(x, p)$ must be a solution of the collisionless Boltzmann equation (also known as Vlasov equation). This implies that $f(x, p)$ should depend on its variables (x, p) only through a constant of motion, such as the total energy.

As a consequence, the distribution function has at least two free parameters with the dimensions of an energy and a

number of particles per unit volume. A natural choice is to consider the hot electron temperature T_e and some reference density (\bar{n}); both these quantities, together with φ^* , enter as free parameters of the model.

Different choices, based either on empirical scaling law or modelling approximations, have been proposed to calculate these quantities from experimental parameters.

A simple choice is to assume that $f(x, p)$ is the Maxwell-Jüttner equilibrium distribution function, where the electron temperature can be evaluated with the well-known ponderomotive scaling [80]:

$$T_e = T_{pm} = m_e c^2 \left(\sqrt{1 + \frac{a_0^2}{2}} - 1 \right) \quad (2)$$

Despite its simplicity, this approach has demonstrated considerable success in reproducing the ion cut-off energies observed in both PIC simulations and experiments when a standard single foil target is considered [79].

However, the simple yet universal character of the ponderomotive scaling cannot take into account the target properties, a key aspect for the modelling on DLT acceleration. Moreover, it is known that ponderomotive scaling tends to overestimate T_e and it is insensitive to other specific features such as laser incidence angle and polarization.

In addition, due to the high non-linearity of superintense laser-matter interaction and the low collisionality of a diluted relativistic electron gas, the assumption of thermodynamic equilibrium for the electron distribution function may not be realistic.

In the following, we propose two complementary strategy to extend the quasi-static TNSA model to a DLT configuration. On the one hand we propose an extension of the ponderomotive scaling for estimating T_e ; on the other hand, we relax the assumption of thermodynamic equilibrium for the electron population by solving the model with a distribution function different from Maxwell-Jüttner.

4.1. Electron heating in DLT configuration

We have studied the hot electron heating by means of a combined numerical and analytical approach for a wide range of laser parameters [81]. Based on our analysis, the electron temperature can be written as a combination of two contributions: the so-called Brunel effect and the $j \times B$ heating, as described by the relation

$$\begin{aligned} T_e [\text{MeV}] = & C_1(a_0, \text{pol}, l_{\text{foil}}) 0.511 \left(\sqrt{1 + \frac{a_0^2}{2}} - 1 \right) \\ & + C_2(a_0, \text{pol}, l_{\text{foil}}) 0.511 \\ & \times \left[\sqrt{1 + f^2 \frac{a_0^2}{2} \sin^2 \theta} - 1 \right] \tan \theta \end{aligned} \quad (3)$$

Where C_1 and C_2 are empirical weighting factors, depending on the system parameters, for the Brunel effect and $j \times B$ heating, respectively, and f is the reflection amplification factor

(approximately equal to 2). These factors can be evaluated by fitting experimental measurements or simulations data; both 2D and 3D PIC simulations were performed to retrieve C_1 and C_2 for standard solid flat targets in a wide range of intensities ($a_0 = 1.5 - 15$, $I = 4.5 \times 10^{18-20} \text{ W cm}^{-2}$). Typical values for p-polarization are $C_1 = 0.2-0.3$ and $C_2 = 0.04-0.06$; for a more detailed discussion the reader should refer to [81].

We extended this approach also to the near-critical DLTs. Through 2D PIC simulations, we studied the effects of the low density layer on the electron temperature starting from a simple and ideal configuration: a homogeneous plasma and fixed angle of incidence (45°). In particular, we fixed the geometry (thicknesses) and we varied the density of the near-critical layer; for each simulation we estimated the temperatures of the hot electrons populations (originating from the substrate and the near-critical layer) as the mean energies of the relativistic electrons, namely the ones with kinetic energy higher than the rest energy (0.511 MeV).

The results of this analysis, reported in figure 6(a), show a characteristic behaviour with respect to electron density in the near-critical layer. Two regimes can be distinguished depending on the parameter \bar{n} as defined in equation (1). When the near-critical plasma is relativistically over-dense ($\bar{n} > 1$ or, equivalently, $n_e > \gamma n_c$), the foam electrons (i.e. electrons from the near-critical layer) are characterized by a sub-ponderomotive temperature well approximated by equation (3), whereas the substrate electrons are significantly colder. Indeed, in this regime the laser is prevented from propagating inside the plasma and reaching the substrate, and it heats the foam electrons with the usual surface mechanisms considered in equation (3).

Conversely, for $\bar{n} < 1$ (or, equivalently, $n_e < \gamma n_c$) the electrons from both the foam and the substrate are heated to super-ponderomotive energies. This can be considered the result of two phenomena taking place when the pulse propagates inside the DLT: on the one hand, foam electrons are accelerated more efficiently by the volumetric heating, on the other hand the laser can undergo self-focusing, thus increasing the intensity at the foam-substrate boundary and ultimately enhancing the temperature of the substrate electrons as well.

It should also be noticed that the mean kinetic energy of the whole (near-critical layer + substrate) hot electron population is well approximated by the near-critical ones alone, due to the fact that those electrons are much more abundant than those coming from the substrate.

Finally, we solved the quasi-static TNSA model by plugging the values of the temperature T_e and the energy conversion efficiency η obtained by the PIC simulations into the scaling laws proposed in [79]. In figure 6(b) we show that the maximum proton energy predicted by the model is in good agreement with the results of PIC simulations. This suggests that the quasi-static model is a useful tool for the evaluation of the proton energy also in the case of DLT configuration.

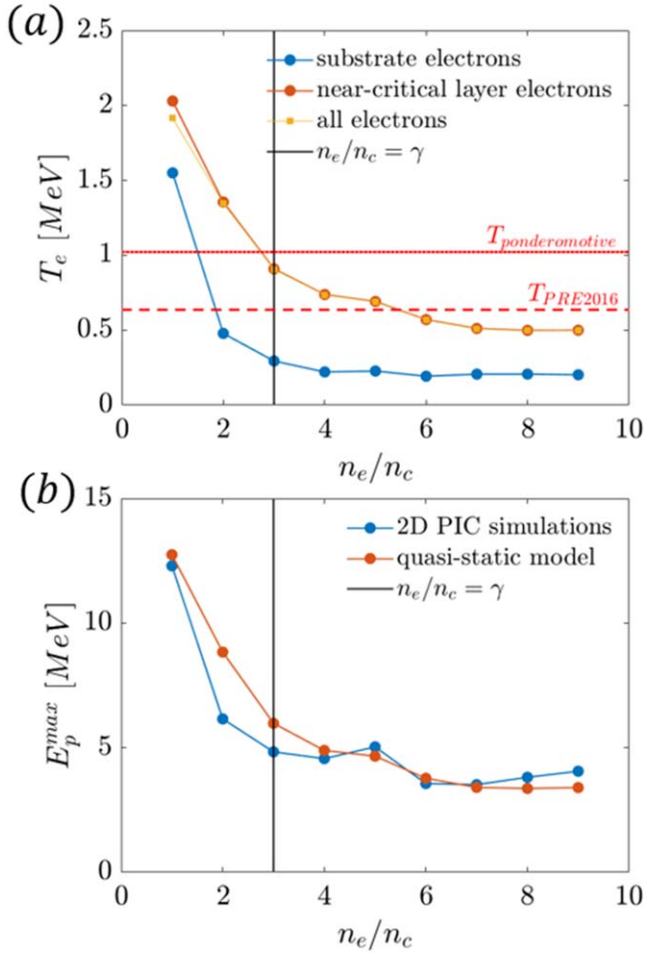


Figure 6. (a) Temperature of different electron population (blue: substrate, red: near-critical layer, yellow: whole target) obtained from 2D PIC simulation of a laser pulse ($a_0 = 4$) interacting with a DLT (homogeneous near-critical layer with 4λ thickness) as a function of the near-critical layer density (in units of critical density n_c). The vertical black line represents the relativistic transparency threshold $n_e\gamma$. The horizontal solid line represents the electron temperature estimated by the ponderomotive scaling [80]. The dashed line is temperature estimated by the scaling proposed in [81]. (b) Maximum proton energies obtained from the same 2D PIC simulations (blue line) and calculated from the 1D, quasi-static TNSA model using the temperature shown in figure 6(a) and the scaling laws proposed in [79] (red line).

4.2. Role of non-thermal electrons in TNSA

In order to study the role and the effect of non-thermal (i.e. out of thermodynamic equilibrium) electrons in TNSA, we performed a 3D PIC simulation where a DLT (homogeneous foam with density $1.5n_c$, thickness 4λ , substrate thickness 0.5λ , $Z/A = 0.5$) has been irradiated at normal incidence with a p-polarized laser ($a_0 = 4$). Figure 7 (blue points) shows the momenta distribution of forward travelling (i.e. $p_x > 0$) electrons from both the foam and the substrate, taken $20 \lambda/c$ after the laser-target interaction has begun.

Data show how the distribution function is well approximated by a Maxwell-Jüttner distribution (green line) for $p_x < 2m_e c$, while there is a significant tail due to out-of-

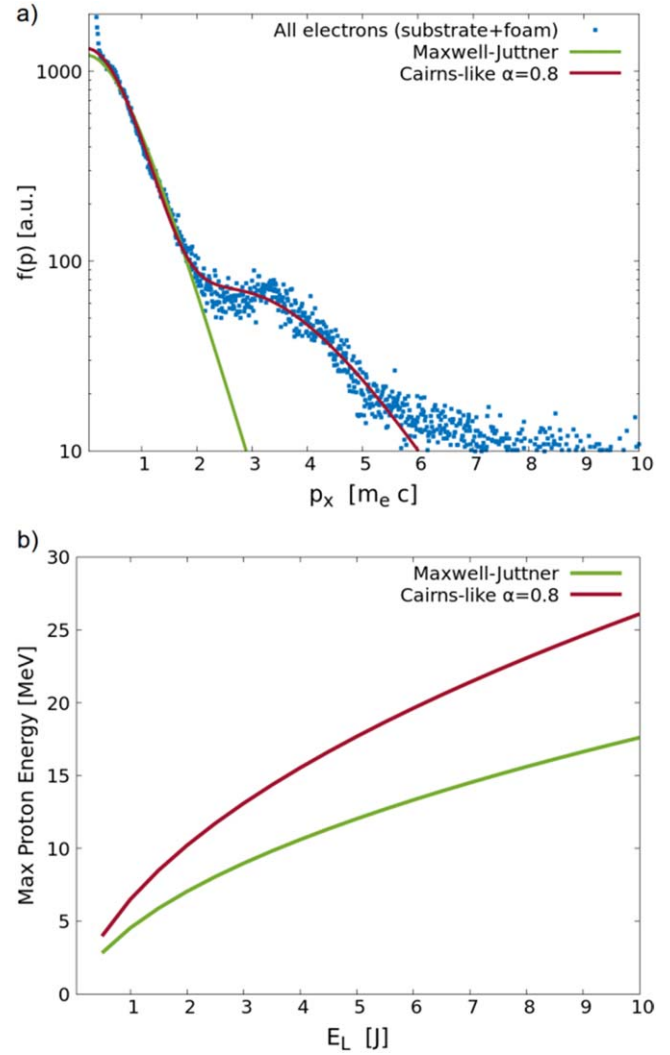


Figure 7 (a) Blue dots: Momenta distribution of forward-moving electrons inside the substrate, as obtained from a 3D PIC simulation ($a_0 = 4$, homogeneous $1.5 n_c$ layer of 4λ thickness in front of a $40n_c$, 0.5λ thick substrate). Green line: Maxwell-Jüttner distribution ($T = 0.22$ MeV) that best fits the PIC data in the interval $[0.5, 5] m_e c$. Red line: Relativistic Cairns-like distribution ($T = 0.36$ MeV, $\alpha = 0.8$) that best fits the PIC data in the interval $[0.5, 5] m_e c$. (b) Maximum proton energies given by the 1D quasi-static TNSA model as a function of laser energy for different distribution functions. Green line: Maxwell-Jüttner distribution. Red line: relativistic Cairns-like distribution, $\alpha = 0.8$.

equilibrium electrons which cannot be accounted for by the equilibrium distribution.

There are several examples of non-equilibrium distribution functions that can be used to describe a non-thermal electron population, such as the Vasyliunas distribution function [82], the Tsallis distribution function [83], a super-Gaussian [84] or a two-temperature Maxwellian function.

The non-relativistic Cairns distribution function [85] has been proposed to describe the non-thermal electrons in TNSA modelling [86] however its non-relativistic character is an intrinsic limitation as far as hot, relativistic electrons are concerned.

Here we make use of a relativistically correct Cairns-like distribution function, namely:

$$f(x, p) = \frac{\tilde{n}}{N(T_e, \alpha)} \left\{ 1 + \alpha \left[\frac{m_e c^2 (\gamma(p) - 1) - e\varphi(x)}{T_e} \right]^2 \right\} \times \exp \left[\frac{-m_e c^2 \gamma(p) + e\varphi(x)}{T_e} \right] \quad (4)$$

$$N(T_e, \alpha) = 2K_1 \left(\frac{m_e c^2}{T_e} \right) + \frac{\alpha m_e^2 c^4}{2T_e^2} \left[-4K_0 \left(\frac{m_e c^2}{T_e} \right) + 7K_1 \left(\frac{m_e c^2}{T_e} \right) - 4K_2 \left(\frac{m_e c^2}{T_e} \right) + K_3 \left(\frac{m_e c^2}{T_e} \right) \right] \quad (5)$$

where $N(T_e, \alpha)$ is the normalization constant (K_i is the Macdonald function of i -th order) which ensures that, for every α , the electron number density $n_e(x) = \int_{-\infty}^{\infty} f(x, p) dp$ is equal to the reference \tilde{n} where the potential vanishes. This function reduces to the Maxwell-Jüttner distribution as α goes to 0, while for $\alpha \rightarrow \infty$ it represents two counter-propagating streams of electrons with momentum equal to $\pm \frac{2}{c} \sqrt{T_e m_e c^2 + T_e^2}$.

The red line in figure 7(a) represents the fitting of the PIC data with the Cairns-like function. It can be seen that a satisfactory agreement is obtained for $\alpha = 0.8$.

In order to assess the effect of the non-equilibrium electrons on the TNSA acceleration, we compare the value of E_p^{\max} predicted by the quasi-static model with the Maxwell-Jüttner and the relativistic Cairns-like distribution for $\alpha = 0.8$. While an analytical solution exists for the former case [8], a numerical integration is required in the latter case. For the sake of simplicity, and to emphasize the role of non-equilibrium, we evaluate T_e and φ^* as a function of the laser energy E_L in the simplest possible way, i.e. by means of the ponderomotive scaling (equation (2)) and the empirical relation proposed in [78] respectively, so that we have the following relations:

$$T_e = m_e c^2 \left(\sqrt{1 + E_L \frac{\lambda^2 m_e c^3}{\sigma \tau}} - 1 \right) \quad (6)$$

$$\varphi^* = T_e (4.8 + 0.8 \log E_L [\text{J}]) \quad (7)$$

where σ and τ are the laser spot size and pulse duration, respectively

The other model parameter \tilde{n} might be used as a degree of freedom to gauge the proton energies; here, we decided to adjust \tilde{n} for varying E_L in order to keep the laser absorption efficiency (i.e. total electron energy divided by E_L) fixed to $\eta = 10\%$.

The model is then solved for $\lambda = 800$ nm, $\sigma = \pi(5\lambda)^2 = 50.26 \mu\text{m}^2$, $\tau = 30$ fs, the corresponding maximum proton energies are shown in figure 7(b). It can be appreciated that, for a given value of laser energy, the proton energy obtained with the Cairns-like function is greater than the corresponding equilibrium value by a factor of about 1.5. These results hint at a role of a super-thermal, non-equilibrium population in the

enhancement of the TNSA process, especially in the case of DLT.

5. Applications of compact laser-driven ion sources

The peculiar properties of laser-driven ion sources (i.e. maximum ion energy up to tens of MeV, ultra-fast bunch duration and high particle density) are of great interest for several applications like materials characterization [1, 27, 87], investigation of materials under plasma irradiation [88, 89], neutron generation [29] and radioisotope production [31, 90]. Systems based on 10 s–100 s TW-class lasers can provide the energy and number of primary particles required by the aforementioned applications.

As extensively discussed in sections 3 and 4, the use of DLTs has already been proven to be a viable route to enhance the acceleration mechanism and allow reaching the necessary number and energy of the accelerated ions for a given application with reduced laser requirements. On the other hand, laser-driven ions present unique features with respect to conventional particle accelerators, where ions are mono-energetic and provided in a continuous beam. Therefore, their compatibility with the applications requirements needs to be properly investigated.

In this section first we present fully 3D PIC simulations campaigns of laser-driven ion acceleration with realistic DLTs to prove the effectiveness of compact setups. Then, we report a theoretical investigation performed with both Geant4 [91] Monte Carlo (MC) simulations and analytical models, with the goal to assess the applicability of DLT-based laser-driven ion sources for neutron generation, Particle Induced x-ray Emission (PIXE) [92] and materials characterization.

5.1. 3D PIC simulations of a compact proton source

We complemented our analytical and semi-analytical activities on enhanced TNSA with fully 3D PIC simulations campaigns with two main goals. First, to study laser-driven ion acceleration with realistic DLTs, made of a near-critical nanostructured layer coupled with a thin solid substrate (in continuity with section 2). Second, to assess the potential of a proton source driven by a compact laser system coupled with nanostructured DLTs.

This numerical simulation campaign is essentially based on the same approach followed in the 3D campaign reported in section 2, but specifically focused on ion acceleration.

In particular, we focused on moderate power (\ll PW) laser systems, which are of interest for a number of potential applications where the actual compactness of the setup is the main appeal (see sections 5.2 and 5.3). To this purpose, we considered a table-top ~ 10 TW laser system and explored to what extent the near-critical layer would improve the accelerated ion properties, i.e. their maximum energy and total number. Overall, we compared four different kinds of target configurations, as shown in figure 8(a): three double-layer targets and a thin solid foil, taken as a reference. As for the three double-layer targets, we modeled the near-critical layer as a homogeneous plasma, a foam-like plasma and a random nanowires array plasma. We

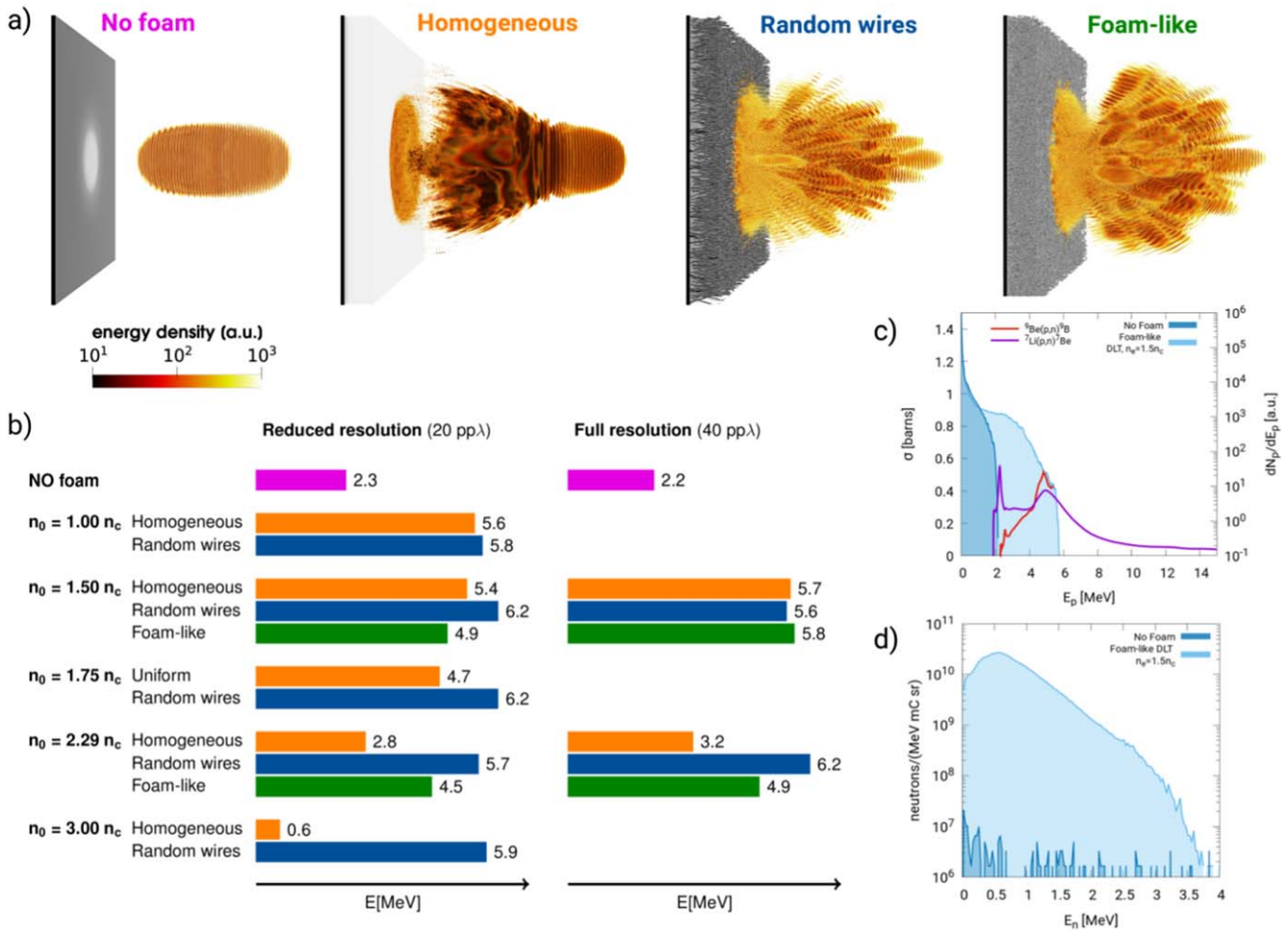


Figure 8. (a) Snapshots from the 3D PIC simulations of laser-driven ion acceleration with different targets: bare solid foil with no attached foam (top left) and three double-layer targets with different near-critical layers: homogeneous, random wires and foam-like. In each plot the energy density of the reflected laser light at time ~ 180 fs is represented in color. (b) table summarizing the maximum proton energies obtained in all the simulations. The main laser parameters are $a_0 = 4$, duration = 30 fs, waist = $4 \mu\text{m}$. (c) Cross-sections (simple lines) of the main proton-induced nuclear reactions to produce neutrons (Beryllium, red and Lithium, purple). All cross-sections are taken from the experimental database EXFOR [93]. Underneath, two proton spectra from 3D PIC simulations are shown as blue filled curves for two kinds of targets: a bare solid foil with no foam (dark) and a foam-attached target (light). (d) Energy spectra of all the neutrons emitted in the 4π solid angle from Geant4 MC simulations of laser-driven neutron sources. The proton bunch from the ‘pitcher’ is sampled from the 3D PIC simulations at full resolution mentioned in panels (a) and (b).

performed several simulations also to explore the sensitivity with respect to variations of the near-critical layer average density. We used two different spatial resolutions: 20 and 40 points per wavelength. This was done for computational reasons: we could explore a wider range of parameters at reduced resolution (20ppλ), while only selected configurations were also simulated at full resolution (40 ppλ). Figure 8(b) shows an overview of the simulations campaign together with the obtained maximum proton energies. All simulations were performed at normal incidence with a transversely Gaussian, longitudinally \cos^2 , P-polarized laser.

As a result, we observed that the near-critical layer leads to a significant enhancement of the maximum proton energy (up to three-fold for the cases at full resolution). Moreover, the nanostructured targets appear to be less sensitive to a density variation if compared to their homogeneous counterparts. Indeed, the campaign at reduced resolution clearly shows that if the near-critical layer is homogeneous and

dense-enough, then the maximum proton energies can become comparable (and even lower) than those obtained with the uncoated target. On the other hand, the nanostructured near-critical layers are more robust with respect to these variations, leading to maximum proton energies with limited deviations. We find these results also in the few simulations at full resolution: increasing the near-critical layer density from $1.5n_c$ to $2.29n_c$ results in a strong reduction of the maximum proton energy with a homogeneous layer (from 5.7 MeV down to 3.2 MeV), whereas a milder effect is observed with the nanostructured layer (see figure 8(b)) [94]. Besides, the results obtained at reduced and full resolution are consistent with each other, which is both a non-trivial and a very convenient outcome.

Now, we can consider the 3D PIC simulations campaigns summarized in this section and those performed to support the experiment presented in section 3.3 in light of the numerical investigations in section 2: two of them correspond to two

different regimes. For instance, \bar{n} (equation (1)) is in the range 0.3–1 in the former, while is 0.1 in the latter. For high \bar{n} (0.3–1) the homogeneous DLT leads to lower proton energies than the nanostructured one, while the opposite occurs at the lower \bar{n} value (0.1). This discrepancy is consistent with the results reported in section 2. At higher \bar{n} , the nanostructured DLTs absorb much more laser energy than the homogeneous DLTs and so they drive the protons to higher energies. On the other hand, at lower \bar{n} , the electrons are heated to higher temperatures with the homogeneous DLT than with the nanostructured one, directly impacting on TNSA.

Our results substantiate the claim for which nanostructured double-layer targets are a promising way to go towards carefully selected applications as discussed in detail in the next sections: they let loosen the laser requirements for a given application, while increasing at the same time the robustness of the scheme against the fluctuation of several parameters (e.g. near-critical layer density and laser polarization).

5.2. Compact laser-driven neutron source

Laser-driven ions may soon find application in the development of neutron sources via (ion,n) reactions. Indeed, the features of laser-driven ion sources are well suited for this application [93, 95, 96].

For instance, many (p,n) reactions have non-vanishing cross sections for proton energies in the range 1–20 MeV (see figure 8(c)), values well within current capabilities of ~ 100 TW-class laser systems. Moreover, there is no special need for either monochromaticity or narrow angular spread of the laser-accelerated ions [97, 98]. Finally, laser-based accelerators might overcome conventional accelerators in terms of flexibility, e.g. in terms of the possibility of controlling and changing both accelerated ions energy and species.

At present day, an appealing challenge would be to achieve that same range of ion energies with lower power systems (~ 10 TW), so to pave the way for the development of secondary sources that are as compact as possible, given nowadays technologies. As far as neutron sources are of concern, besides the potential compactness, laser-driven neutron sources would be appealing also because of their pulsed nature and ultra-fast dynamics (~ 10 ps–ns) [29, 99]. Up to now, yields per shot of interest ($\sim 10^4$ – 10^{10} n/shot) have already been reported in the literature, using (p,n), (d,n) or photo-nuclear reactions [29, 99, 100]. However, very few works have employed table-top lasers [101–103].

Within this picture, the design of laser-driven neutron sources would greatly benefit from a complete theoretical description of the whole process, from laser-target interaction to secondary particles generation and transport. We worked towards this direction by combining numerical and analytical investigations in order to provide a first feasibility study, also exploiting the potential advantages offered by DLT solutions [98, 104, 105].

Here we focus on the generation of neutrons using a pitcher-catcher configuration, where the catcher plays the role of a proton-to-neutron converter via proton-induced nuclear reactions.

In a first investigation [98] we examined the role of several converter properties by means of both Geant4 [91]

Monte Carlo simulations and analytical estimations. Indeed, in order to optimize the neutron spectrum in view of a certain application, the choice of the converter material is crucial. At the same time, possible handling prescriptions and issues due to the operational conditions (e.g. melting) should be considered. When protons or deuterons are accelerated, the most widely used converter materials are lithium and beryllium [96, 106–108].

Both of them have drawbacks and advantages. For example, albeit Li leads to the highest neutron yields, it is less resistant to thermal loads if compared to Be. However, both Be and Li are affected by hydrogen embrittlement. In any case, the optimal catcher configuration depends on the specific properties of the impinging ions.

Another important property of the converter is its thickness. In [98] we found that the optimal thickness of the converter is equal to the range of the most energetic incoming ions: if thinner, then not all the protons are converted, if thicker it may result in a lower degree of collimation, which may not be desired in experiments.

Based on these preliminary investigations, we numerically tested how the compact laser-driven proton source modelled in the previous section would behave if used to generate neutrons. We chose to consider pure beryllium with thickness equal to the range of the highest energy accelerated protons. This means relying mainly on the endothermic reaction ${}^9\text{Be} + \text{p} \rightarrow {}^9\text{B} + \text{n}$, which has a threshold of ~ 2 MeV and a Q-value of -1.85 MeV. We simulated neutron generation under these conditions by means of MC simulations with the Geant4 code. We coupled our 3D PIC simulations of laser-driven ion acceleration mentioned in section 5.1 with the MC code: the momentum distribution of the incident proton bunch in the MC simulations is directly sampled from the phase space of the accelerated ions obtained as an output of the 3D PIC simulations. We recall that in those simulations the laser is representative of a ~ 10 TW system with 30 fs duration, $4 \mu\text{m}$ waist and a peak normalized vector potential of $a_0 = 4$. Of course, in order to actually generate neutrons, it is crucial that the projectile protons overcome the reaction threshold. We find that with a simple solid foil the maximum ion energy barely exceeds the reaction threshold, which leads to the generation of a low amount of neutrons, with a conversion rate of $\sim 10^{-8}$ n/p. However, with foam-attached targets like those mentioned in section 5.1, the threshold is satisfactorily exceeded (see figure 8(c)). For example, with a DLT with a foam-like near-critical layer and density $n_e = 1.5 n_c$, we obtain a conversion rate of $\sim 5 \times 10^{-5}$ n/p. In this scenario, if compared to the bare solid foil, the foam-target enables the neutron generation process, which also greatly benefits from the increased number of accelerated protons. In figure 8(d) we show the energy spectra of the neutrons emitted in the 4π solid angle, for a fixed number of projectile protons (10^{10}) with energy above the threshold. It is clear the great advantage in terms of neutron yield given by the foam target. For more details about how other DLT morphologies would perform for secondary neutron generation please refer to [94].

5.3. Laser-driven PIXE

PIXE is part of the Ion Beam Analysis (IBA) [92, 109] family of techniques for materials characterization. IBA relies on the irradiation of samples with monoenergetic ion beams (few MeV/u of energy). Characteristic radiation is emitted when the impinging ions interact with the atoms (or nuclei) of the sample. Knowledge of the number and energy of secondary particles can allow reconstructing the elemental composition of the sample. At present, IBA techniques are widely exploited in biochemistry [110], electronics [111] and cultural heritage studies [112]. The more widespread systems to perform IBA studies are Van de Graff and Tandem accelerators [92]. These machines represent the oldest accelerator technology and, as a consequence, they are affected by several limitations: high cost of purchase and maintenance, big size, non-tunability of the particle energy and radioprotection issues. As far as PIXE is concerned, the impinging particles are generally protons and the emitted characteristic radiation consists in x-rays. The x-ray energies can be directly related to the chemical elements in the sample. Besides, by means of commercial codes, the x-ray peak intensities can be correlated to the elemental concentrations. Protons interacting with electrons of the sample undergo very small changes of their propagation direction. Therefore, their trajectories are essentially linear. As a result, a particular PIXE variant, namely Differential PIXE, can be exploited to retrieve information at different depths [113, 114]. The aforementioned codes rely on a well-known theoretical model [92]. Starting from the incident proton energy and the irradiation geometry, the model associates the number of detected x-rays to the sample composition, without the need of reference samples.

In order to demonstrate the potentials of PIXE using laser-driven protons, in a very recent paper [1] we presented a detailed theoretical-numerical investigation of this technique. Firstly, we extended the known theoretical model for the description of PIXE [114] allowing for a non-monoenergetic proton spectrum, which is obtained by modelling a realistic laser-driven ion source with a double-layer target. We also developed an iterative code for laser-driven PIXE quantitative analysis (i.e. the elemental concentrations and concentration depth profiles reconstruction). To test our code, we performed a series of Geant4 MC simulations of laser-driven PIXE experiments. In particular, we simulated irradiation of complex samples, representative of cultural heritage artifacts with different laser-driven proton sources (pure exponential energy spectra and spectra retrieved from 3D PIC simulations), as well as generation and detection of the emitted x-rays. The simulated x-ray intensities have been processed with the developed code in order to reconstruct the sample composition. In all cases, the agreement between the reconstructed composition and the sample concentration set in the MC simulation was confirmed. It is important to mention that the PIC simulated proton sources (cut-off energies from 2 to 6 MeV and 10^8 – 10^9 protons per bunch) including the presence of a DLT (with a homogeneous near-critical layer) are compatible with compact 10 s TW-class laser systems.

Here we want to address theoretically a further important aspect, not considered so far in our previous works, related to the fact that, together with protons, laser-driven ion sources

accelerate also a large amount of electrons. This point is important because, if not properly removed, electrons might affect the result of a laser-driven PIXE measurement.

We present MC simulations of sample irradiation with protons and electrons, considering both in-vacuum and in-air sample irradiation setups. A comprehensive scheme for the second case is shown in figure 9(a). The particles are generated 4 cm far from the sample. The energy spectra are purely exponential, with temperatures of 0.7 MeV and 5 MeV, cut-off energies of 5 MeV and 15 MeV for protons and electrons respectively. Their angular divergence with respect to the normal of the sample surface is uniformly distributed between $\pm 10^\circ$ for the protons and $\pm 20^\circ$ for the electrons. These parameters are coherent to those reported in [1]. 10^9 protons and 10^8 electrons have been simulated. Before reaching the sample, primary particles pass through a 10 μm aluminum film. The sample is composed by a 2.25 μm thick superficial layer of Cr and a 1 mm thick substrate of Cu. Finally, the simulation setup includes a detection screen (2.5×2.5 cm) for the x-rays placed 5 cm far from the sample.

As far as the protons are concerned, a detailed description of the physical processes implemented in the MC simulations is provided in [1]. For the electrons, we here enable the Penelope low-energy electromagnetic models available with the Geant4 toolkit [115].

Figure 9(b) shows the x-ray spectra recorded on the detector screen in the 1–11 keV energy range with the in-air irradiation setup, normalized with respect to the number of incident proton/electron. The light blue filled spectrum is obtained with electron irradiation, while the dark blue line represents the PIXE spectrum, i.e. from pure proton irradiation. It is clear that the x-ray emission due to the electrons covers the PIXE spectrum completely, both in terms of characteristic peaks and background. Moreover, the bremsstrahlung background extends in the MeV energy range (see figure 9(c)).

Figure 9(d) reports the x-ray peaks intensities for protons and electrons irradiation as obtained in vacuum and in air PIXE setup. With the electron irradiation, the x-ray yields are two orders of magnitude higher with respect to proton irradiation, both in vacuum and in air conditions.

These results definitely show that, if not properly removed, electrons can irreparably distort the result of a PIXE measurement. Therefore, in order to perform laser-driven PIXE, the removal of the electrons is absolutely mandatory. This can be done exploiting a sufficiently intense magnetic dipole (fraction of Tesla) as successfully tested in several experiments [116–118].

Anyway, the presence of a mixed field of ions and electrons is a peculiar property of laser-driven sources, not shared by conventional accelerators, which could be exploited for material analysis purposes. First of all, we notice that the x-ray yields generated by laser-driven electrons are exceptionally high, paving the way to a powerful detection capability for trace elements. Moreover, conversely to the state of the art EDXS analysis with conventional electron sources, which exploits keV energy electrons to irradiate samples of unknown composition and generate characteristic x-rays (see section 3.1 for details), the energies of laser-driven electrons extend in the MeV energy range. This could open up to the analysis of samples exploiting electron beams also in air, since MeV electrons have very long path

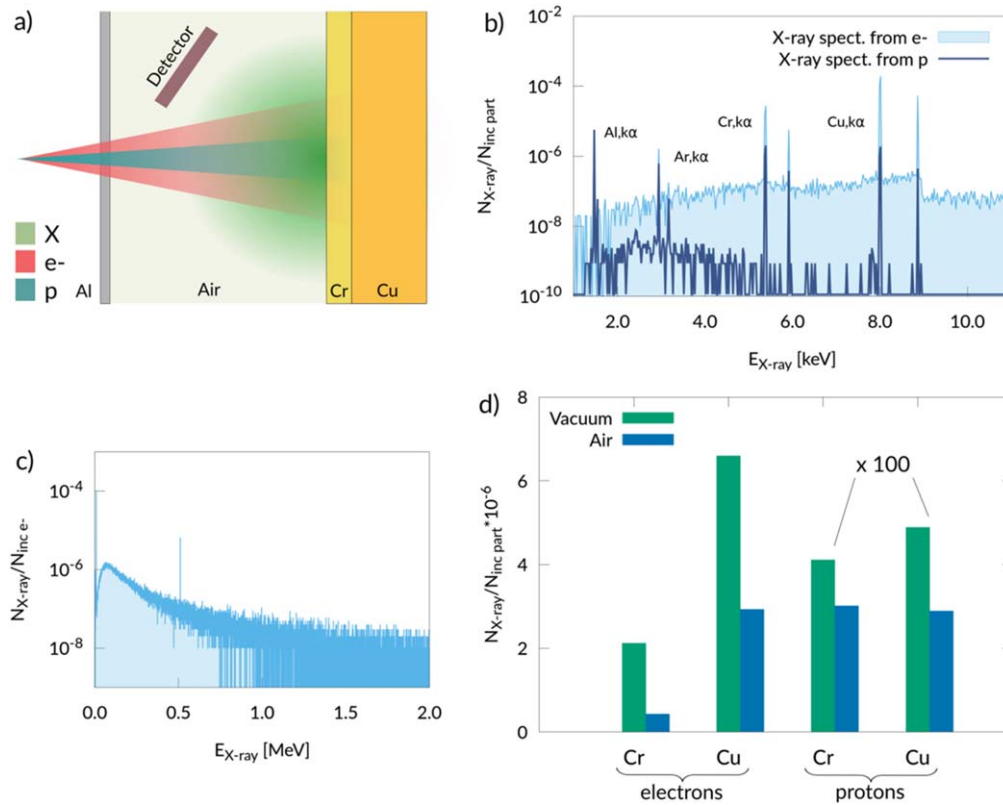


Figure 9. (a) Simulation experimental setup for laser-driven PIXE in air. (b) Low energy part of the x-ray spectra obtained from proton (dark blue line) and electron (light blue filled line) irradiation in air. (c) X-ray spectrum obtained from electron irradiation in the 0–2 MeV energy range. (d) X-ray yields for Cr and Cu for protons and electrons irradiation, in vacuum and in air PIXE setup.

length (100 s cm in air). On the other hand, the material analysis based on laser-generated electrons irradiation presents some additional difficulties with respect to laser-driven PIXE. In fact, the long electrons path (several mm in solids), the unpredictability of trajectories and the generation of secondaries (δ -rays) capable of inducing ionization do not allow easily developing a quantitative analysis and retrieve sample composition.

6. Conclusions

In this paper we have presented the main results and most recent advances of the ERC project ENSURE in the field of laser-driven ion sources and their applications in materials/nuclear science and engineering. The project ultimately aims to develop strategies to produce compact and flexible laser-driven ion accelerators to be used for ion beam analysis, neutron generation and radioisotope production. In order to go towards such main goals, a key aspect is the development of expertise and techniques for the manufacturing of advanced targets with controlled properties at the micro/nanometric scale, together with an improvement in the theoretical understanding of the relevant ion acceleration regimes. In particular, by combining suitable theoretical and experimental tools, the focus is mainly on the study, design and production of near-critical, nanostructured, double-layer targets, exploited to drive an enhanced ion acceleration process. In the final part of the project we will further experimentally investigate laser-driven ion acceleration with

DLT, extending the range of considered laser and target parameters and supporting the activities with the developed theoretical models. In particular, we aim to exploit the novel DLT concepts described in this paper. As far as laser-driven PIXE is concerned, we started addressing it experimentally, in order to assess its feasibility and potentials. We are also studying other appealing applications of laser-driven ion sources such as laser-driven nuclear reaction analysis (NRA) and radioisotope production. The research program naturally requires the establishment of a team having a strong interdisciplinary character and the adoption of non-conventional, innovative experimental and theoretical approaches. More generally, the development of this project can stimulate research on laser-driven ion acceleration, providing new directions to attain concrete applications of relevance, in the near future. Finally, we believe that its approaches and outcomes could be of interest in other contexts as well, for instance in the fundamental physics of laser-plasma interaction and in the production of other laser-plasma based secondary radiation. In this regard, the outcomes of ENSURE can also support the development of expertise required for research on major European infrastructures active in this field.

Acknowledgments

This project has received funding from the European Research Council (ERC) under the European Union's Horizon 2020 research and innovation programme (ENSURE

grant agreement No. 647554 and INTER grant agreement No. 754916). We also acknowledge LISA and Iskra access schemes to MARCONI HPC machine at CINECA(Italy) via the projects LAST, LIRF and EneDaG. We also acknowledge LISA, Iskra and PRACE access schemes to the HPC resources available at CINECA(Italy) via the projects: LAST, LIRF, EneDaG, SNAP, LIonFAT, LaCoSa, LAPLAST, LSAIL.

ORCID iDs

M Passoni  <https://orcid.org/0000-0002-7844-3691>
 D Dellasega  <https://orcid.org/0000-0002-7389-9307>
 L Fedeli  <https://orcid.org/0000-0002-7215-4178>
 A Maffini  <https://orcid.org/0000-0002-3388-5330>
 F Mirani  <https://orcid.org/0000-0002-9789-0075>
 A Pazzaglia  <https://orcid.org/0000-0001-7486-2576>
 M Zavelani-Rossi  <https://orcid.org/0000-0001-9910-0391>
 V Russo  <https://orcid.org/0000-0001-9543-0422>

References

- [1] Passoni M, Fedeli L and Mirani F 2019 Superintense laser-driven ion beam analysis *Sci. Rep.* **9** 9202
- [2] Macchi A, Borghesi M and Passoni M 2013 Ion acceleration by superintense laser-plasma interaction *Rev. Mod. Phys.* **85** 751–93
- [3] Daido H, Nishiuchi M and Pirozhkov A S 2012 Review of laser-driven ion sources and their applications *Reports Prog. Phys.* **75** 056401
- [4] Schreiber J, Bolton P R and Parodi K 2016 Invited review article: ‘hands-on’ laser-driven ion acceleration: a primer for laser-driven source development and potential applications *Rev. Sci. Instrum.* **87** 071101
- [5] Wilks S C, Langdon A B, Cowan T E, Roth M, Singh M, Hatchett S, Key M H, Pennington D, MacKinnon A and Snavely R A 2001 Energetic proton generation in ultra-intense laser–solid interactions *Phys. Plasmas* **8** 542–9
- [6] Scullion C *et al* 2017 Polarization dependence of bulk ion acceleration from ultrathin foils irradiated by high-intensity ultrashort laser pulses *Phys. Rev. Lett.* **119** 054801
- [7] Haberberger D, Tochitsky S, Fiuza F, Gong C, Fonseca R A, Silva L O, Mori W B and Joshi C 2012 Collisionless shocks in laser-produced plasma generate monoenergetic high-energy proton beams *Nat. Phys.* **8** 95–9
- [8] Passoni M, Bertagna L and Zani A 2010 Target normal sheath acceleration: theory, comparison with experiments and future perspectives *New J. Phys.* **12** 045012
- [9] Borghesi M and Schramm U 2016 Summary of working group 2: ion beams from plasmas *Nucl. Instruments Methods Phys. Res. Sect. A Accel. Spectrometers, Detect. Assoc. Equip.* **829** 137–40
- [10] Danson C, Hillier D, Hopps N and Neely D 2015 Petawatt class lasers worldwide *High Power Laser Sci. Eng.* **3** e3
- [11] Danson C N *et al* 2019 Petawatt and exawatt class lasers worldwide *High Power Laser Sci. Eng.* **7** e54
- [12] Palmer C 2018 Paving the way for a revolution in high repetition rate laser-driven ion acceleration *New J. Phys.* **20** 061001
- [13] Morrison J T, Feister S, Frische K D, Austin D R, Ngirmang G K, Murphy N R, Orban C, Chowdhury E A and Roquemore W M 2018 MeV proton acceleration at kHz repetition rate from ultra-intense laser liquid interaction *New J. Phys.* **20** 022001
- [14] Prencipe I *et al* 2017 Targets for high repetition rate laser facilities: needs, challenges and perspectives *High Power Laser Sci. Eng.* **5** e17
- [15] Szerypo J *et al* 2019 Target fabrication for laser-ion acceleration research at the technological laboratory of the LMU munich *Matter Radiat. Extrem.* **4** 035201
- [16] Willingale L, Nilson P M, Thomas A G R, Bulanov S S, Maksimchuk A, Nazarov W, Sangster T C, Stoeckl C and Krushelnick K 2011 High-power, kilojoule laser interactions with near-critical density plasma *Phys. Plasmas* **18** 056706
- [17] Sgattoni A, Londrillo P, Macchi A and Passoni M 2012 Laser ion acceleration using a solid target coupled with a low-density layer *Phys. Rev. E* **85** 036405
- [18] Bin J H H *et al* 2018 Enhanced laser-driven ion acceleration by superponderomotive electrons generated from near-critical-density plasma *Phys. Rev. Lett.* **120** 074801
- [19] Fedeli L, Formenti A, Cialfi L, Pazzaglia A and Passoni M 2018 Ultra-intense laser interaction with nanostructured near-critical plasmas *Sci. Rep.* **8** 3834
- [20] Fedeli L, Formenti A, Bottani C E and Passoni M 2017 Parametric investigation of laser interaction with uniform and nanostructured near-critical plasmas *Eur. Phys. J. D* **71** 202
- [21] Zani A, Dellasega D, Russo V and Passoni M 2013 Ultra-low density carbon foams produced by pulsed laser deposition *Carbon N Y* **56** 358–65
- [22] Nagai K, Musgrave C S A and Nazarov W 2018 A review of low density porous materials used in laser plasma experiments *Phys. Plasmas* **25** 030501
- [23] Ma W *et al* 2007 Directly synthesized strong, highly conducting, transparent single-walled carbon nanotube films *Nano Lett.* **7** 2307–11
- [24] Sylla F, Veltcheva M, Kahaly S, Flacco A and Malka V 2012 Development and characterization of very dense submillimetric gas jets for laser-plasma interaction *Rev. Sci. Instrum.* **83** 033507
- [25] Nakamura T, Tampo M, Kodama R, Bulanov S V and Kando M 2010 Interaction of high contrast laser pulse with foam-attached target *Phys. Plasmas* **17** 113107
- [26] Passoni M, Zani A, Sgattoni A, Dellasega D, Macchi A, Prencipe I, Floquet V, Martin P, Liseykina T V V and Ceccotti T 2014 Energetic ions at moderate laser intensities using foam-based multi-layered targets *Plasma Phys. Control. Fusion* **56** 045001
- [27] Barberio M, Veltri S, Scisciò M and Antici P 2017 Laser-accelerated proton beams as diagnostics for cultural heritage *Sci. Rep.* **7** 40415
- [28] Lancaster K L *et al* 2004 Characterization of $7\text{Li}(p,n)7\text{Be}$ neutron yields from laser produced ion beams for fast neutron radiography *Phys. Plasmas* **11** 3404–8
- [29] Roth M *et al* 2013 Bright laser-driven neutron source based on the relativistic transparency of solids *Phys. Rev. Lett.* **110** 044802
- [30] Lefebvre E, D’Humières E, Fritzier S and Malka V 2006 Numerical simulation of isotope production for positron emission tomography with laser-accelerated ions *J. Appl. Phys.* **100** 113308
- [31] Ledingham K W D *et al* 2004 High power laser production of short-lived isotopes for positron emission tomography *J. Phys. D: Appl. Phys.* **37** 2341–5
- [32] ERC ENSURE webpage (<https://www.ensure.polimi.it/>)
- [33] Chen L M *et al* 2010 Intense high-contrast femtosecond K-shell x-ray source from laser-driven Ar clusters *Phys. Rev. Lett.* **104** 215004
- [34] Andriyash I A, Lehe R, Lifschitz A, Thaury C, Rax J-M, Krushelnick K and Malka V 2014 An ultracompact x-ray source based on a laser-plasma undulator *Nat. Commun.* **5** 4736
- [35] Mondal S *et al* 2017 Aligned copper nanorod arrays for highly efficient generation of intense ultra-broadband THz pulses *Sci. Rep.* **7** 40058

- [36] Fedeli L, Formenti A, Cialfi L, Sgattoni A, Cantono G and Passoni M 2018 Structured targets for advanced laser-driven sources *Plasma Phys. Control. Fusion* **60** 014013
- [37] Cantono G, Fedeli L, Sgattoni A, Denoed A, Chopineau L, Réau F, Ceccotti T and Macchi A 2018 Extreme ultraviolet beam enhancement by relativistic surface plasmons *Phys. Rev. Lett.* **120** 264803
- [38] Martínez B, D'Humières E and Gremillet L 2018 Synchrotron emission from nanowire array targets irradiated by ultraintense laser pulses *Plasma Phys. Control. Fusion* **60** 074009
- [39] Willingale L *et al* 2009 Characterization of high-intensity laser propagation in the relativistic transparent regime through measurements of energetic proton beams *Phys. Rev. Lett.* **102** 125002
- [40] Passoni M *et al* 2016 Toward high-energy laser-driven ion beams: nanostructured double-layer targets *Phys. Rev. Accel. Beams* **19** 061301
- [41] Prencipe I *et al* 2016 Development of foam-based layered targets for laser-driven ion beam production *Plasma Phys. Control. Fusion* **58** 034019
- [42] Bin J H *et al* 2015 Ion acceleration using relativistic pulse shaping in near-critical-density plasmas *Phys. Rev. Lett.* **115** 064801
- [43] Fedeli L *et al* 2016 Electron acceleration by relativistic surface plasmons in laser-grating interaction *Phys. Rev. Lett.* **116** 015001
- [44] Purvis M A *et al* 2013 Relativistic plasma nanophotonics for ultrahigh energy density physics *Nat. Photonics* **7** 796–800
- [45] Bargsten C *et al* 2017 Energy penetration into arrays of aligned nanowires irradiated with relativistic intensities: Scaling to terabar pressures *Sci. Adv.* **3** e1601558
- [46] Jeevanandam J, Barhoum A, Chan Y S, Dufresne A and Danquah M K 2018 Review on nanoparticles and nanostructured materials: history, sources, toxicity and regulations *Beilstein J. Nanotechnol.* **9** 1050–74
- [47] Rosmej O N *et al* 2019 Interaction of relativistically intense laser pulses with long-scale near critical plasmas for optimization of laser based sources of MeV electrons and gamma-rays *New J. Phys.* **21** 043044
- [48] Willingale L *et al* 2018 The unexpected role of evolving longitudinal electric fields in generating energetic electrons in relativistically transparent plasmas *New J. Phys.* **20** 093024
- [49] Kim I, Choi I W, Lee S K, Janulewicz K A, Sung J H, Yu T J, Kim H T, Yun H, Jeong T M and Lee J 2011 Spatio-temporal characterization of double plasma mirror for ultrahigh contrast and stable laser pulse *Appl. Phys. B* **104** 81–6
- [50] Schramm U *et al* 2017 First results with the novel petawatt laser acceleration facility in Dresden *J. Phys. Conf. Ser.* **874** 012028
- [51] Ditmire T, Donnelly T, Rubenchik A M, Falcone R W and Perry M D 1996 Interaction of intense laser pulses with atomic clusters *Phys. Rev. A* **53** 3379–402
- [52] Arber T D *et al* 2015 Contemporary particle-in-cell approach to laser-plasma modelling *Plasma Phys. Control. Fusion* **57** 113001
- [53] Okihara S *et al* 2004 Ion generation in a low-density plastic foam by interaction with intense femtosecond laser pulses *Phys. Rev. E - Stat. Nonlinear, Soft Matter Phys.* **69** 026401
- [54] Sgattoni A, Fedeli L and Sinigardi S 2014 *Optimising PICCANTE - an Open Source Particle-in-Cell Code for Advanced Simulations on Tier-0 Systems* (<https://arxiv.org/abs/1503.02464>)
- [55] Kaw P and Dawson J 1970 Relativistic nonlinear propagation of laser beams in cold overdense plasmas *Phys. Fluids* **13** 472–81
- [56] Akhiezer A and Polovin R V 1956 Theory of wave motion of an electron *Plasma J. Exp. Theoretical Phys.* **3** 696
- [57] Palaniyappan S *et al* 2012 Dynamics of relativistic transparency and optical shattering in expanding overdense plasmas *Nat. Phys.* **8** 763–9
- [58] Pukhov A, Sheng Z-M and Meyer-ter-Vehn J 1999 Particle acceleration in relativistic laser channels *Phys. Plasmas* **6** 2847–54
- [59] Gauthier M *et al* 2017 High repetition rate, multi-MeV proton source from cryogenic hydrogen jets *Appl. Phys. Lett.* **111** 114102
- [60] Thales TeraWatt Systems (<https://www.thalesgroup.com/en/worldwide/group/market-specific-solutions-lasers-science-applications/terawatt-systems>)
- [61] Ma W J *et al* 2019 Laser acceleration of highly energetic carbon ions using a double-layer target composed of slightly underdense plasma and ultrathin foil *Phys. Rev. Lett.* **122** 014803
- [62] Chrisey D B and Hubler G K 2006 *Pulsed Laser Deposition of Thin Films (Pulsed Laser Deposition of Thin Films)* (New York: Wiley)
- [63] Pazzaglia A, Maffini A, Dellasega D, Lamperti A and Passoni M 2019 Reference-free evaluation of thin films mass thickness and composition through energy dispersive x-ray spectroscopy *Mater. Charact.* **153** 92–102
- [64] Prencipe I, Dellasega D, Zani A, Rizzo D and Passoni M 2015 Energy dispersive x-ray spectroscopy for nanostructured thin film density evaluation *Sci. Technol. Adv. Mater.* **16** 025007
- [65] Maffini A, Pazzaglia A, Dellasega D, Russo V and Passoni M 2019 On the growth dynamics of pulsed laser deposited nanofoams *Phys. Rev. Mater.* **3** 083404
- [66] Witten T A and Sander L M 1981 Diffusion-limited aggregation, a kinetic critical phenomenon *Phys. Rev. Lett.* **47** 1400–3
- [67] Meakin P and Stanley H E 1983 Spectral dimension for the diffusion-limited aggregation model of colloid growth *Phys. Rev. Lett.* **51** 1457–60
- [68] Gao B, Zhang S, Ju X, Lin Y and Wang X 2017 Femtosecond pulsed laser deposition of nanostructured TiO₂ films in atmosphere *AIP Adv.* **7** 095206
- [69] Sung J H, Lee S K, Yu T J, Jeong T M and Lee J 2010 0.1 Hz 10 PW Ti:sapphire laser *Opt. Lett.* **35** 3021
- [70] Spindloe C, Arthur G, Hall F, Tomlinson S, Potter R, Kar S, Green J, Higginbotham A, Booth N and Tolley M K 2016 High volume fabrication of laser targets using MEMS techniques *J. Phys. Conf. Ser.* **713** 012002
- [71] Miyamoto Y, Fujii Y, Yamano M, Harigai T, Suda Y, Takikawa H, Kawano T, Nishiuchi M, Sakaki H and Kondo K 2016 Preparation of self-supporting Au thin films on perforated substrate by releasing from water-soluble sacrificial layer *Jpn. J. Appl. Phys.* **55** 07LE05
- [72] Kelly P and Arnell R 2000 Magnetron sputtering: a review of recent developments and applications *Vacuum* **56** 159–72
- [73] Sarakinos K, Alami J and Konstantinidis S 2010 High power pulsed magnetron sputtering: a review on scientific and engineering state of the art *Surf. Coatings Technol.* **204** 1661–84
- [74] Thornton J A 1974 Influence of apparatus geometry and deposition conditions on the structure and topography of thick sputtered coatings *J. Vac. Sci. Technol.* **11** 666–70
- [75] Anders A 2010 A structure zone diagram including plasma-based deposition and ion etching *Thin Solid Films* **518** 4087–90
- [76] Vavassori D 2019 *Production of Optimized Targets for Enhanced Laser-driven Ion Acceleration* Politecnico di Milano (<http://hdl.handle.net/10589/148398>)
- [77] Zeil K, Kraft S D, Bock S, Bussmann M, Cowan T E, Kluge T, Metzkes J, Richter T, Sauerbrey R and Schramm U 2010 The scaling of proton energies in ultrashort pulse laser plasma acceleration *New J. Phys.* **12** 045015

- [78] Passoni M and Lontano M 2008 Theory of light-ion acceleration driven by a strong charge separation *Phys. Rev. Lett.* **101** 115001
- [79] Passoni M, Perego C, Sgattoni A and Batani D 2013 Advances in target normal sheath acceleration theory *Phys. Plasmas* **20** 060701
- [80] Wilks S C and Kruer W L 1997 Absorption of ultrashort, ultra-intense laser light by solids and overdense plasmas *IEEE J. Quantum Electron.* **33** 1954–68
- [81] Cialfi L, Fedeli L and Passoni M 2016 Electron heating in subpicosecond laser interaction with overdense and near-critical plasmas *Phys. Rev. E* **94** 053201
- [82] Vasyliunas V M and Siscoe G L 1976 On the flux and the energy spectrum of interstellar ions in the solar system *J. Geophys. Res.* **81** 1247–52
- [83] Douglas P, Bergamini S and Renzoni F 2006 Tunable Tsallis Distributions in Dissipative Optical Lattices *Phys. Rev. Lett.* **96** 110601
- [84] Fourkal E, Bychenkov V Y, Rozmus W, Sydora R, Kirkby C, Capjack C E, Glenzer S H and Baldis H A 2001 Electron distribution function in laser heated plasmas *Phys. Plasmas* **8** 550–6
- [85] Cairns R A, Mamun A A, Bingham R, Boström R, Dendy R O, Nairn C M C and Shukla P K 1995 Electrostatic solitary structures in non-thermal plasmas *Geophys. Res. Lett.* **22** 2709–12
- [86] Bahache A, Bennaceur-Doumaz D and Djebli M 2017 Effects of energetic electrons on ion acceleration in a quasi-static model *Phys. Plasmas* **24** 083102
- [87] Barberio M and Antici P 2019 Laser-PIXE using laser-accelerated proton beams *Sci. Rep.* **9** 6855
- [88] Maffini A, Moser L, Marot L, Steiner R, Dellasega D, Uccello A, Meyer E and Passoni M 2017 In Situ Cleaning of Diagnostic First Mirrors: an Experimental Comparison Between Plasma and Laser Cleaning in ITER-relevant Conditions *Nucl. Fusion* **57** 046014
- [89] Besozzi E, Maffini A, Dellasega D, Russo V, Facibeni A, Pazzaglia A, Beghi M G and Passoni M 2018 Nanosecond laser pulses for mimicking thermal effects on nanostructured tungsten-based materials *Nucl. Fusion* **58** 036019
- [90] Luo W, Bobeica M, Gheorghie I, Filipescu D M, Niculae D and Balabanski D L 2016 Estimates for production of radioisotopes of medical interest at Extreme Light Infrastructure—Nuclear Physics facility *Appl. Phys. B* **122** 8
- [91] Allison J *et al* 2016 Recent developments in Geant4 *Nucl. Instruments Methods Phys. Res. Sect. A Accel. Spectrometers, Detect. Assoc. Equip.* **835** 186–225
- [92] Hoffmann P 2008 H.R. Verma: Atomic and nuclear analytical methods. XRF, Mössbauer, XPS, NAA and ion-beam spectroscopic techniques *Anal. Bioanal. Chem.* **391** 2103–4
- [93] Alejo A, Ahmed H, Green A, Mirfayzi S R, Borghesi M and Kar S 2015 Recent advances in laser-driven neutron sources *Nuovo Cim. della Soc. Ital. di Fis. C* **38** 188
- [94] Fedeli L, Formenti A, Pazzaglia A, Arioli F, Tentori A and Passoni M 2019 Enhanced laser-driven hadron sources with nanostructured double-layer targets *New J. Phys.*
- [95] Alvarez J, Fernández-Tobias J, Mima K, Nakai S, Kar S, Kato Y and Perlado J M 2014 Laser driven neutron sources: characteristics, applications and prospects *Phys. Proc.* (Elsevier B.V.) **60** 29–38
- [96] Brenner C M *et al* 2015 Laser-driven x-ray and neutron source development for industrial applications of plasma accelerators *Plasma Phys. Control. Fusion* **58** 014039
- [97] Petrov G M, Higginson D P, Davis J, Petrova T B, McGuffey C, Qiao B and Beg F N 2013 Generation of energetic (>15 MeV) neutron beams from proton- and deuterium-driven nuclear reactions using short pulse lasers *Plasma Phys. Control. Fusion* **55** 105009
- [98] Arioli F M 2018 *Compact Laser-driven Neutron Sources: a Theoretical Investigation* Politecnico di Milano (<http://hdl.handle.net/10589/142386>)
- [99] Pomerantz I *et al* 2014 Ultrashort pulsed neutron source *Phys. Rev. Lett.* **113** 184801
- [100] Kar S *et al* 2016 Beamed neutron emission driven by laser accelerated light ions *New J. Phys.* **18** 053002
- [101] Zulick C *et al* 2013 Energetic neutron beams generated from femtosecond laser plasma interactions *Appl. Phys. Lett.* **102** 124101
- [102] Jiao X J *et al* 2017 A tabletop, ultrashort pulse photoneutron source driven by electrons from laser wakefield acceleration *Matter Radiat. Extrem.* **2** 296–302
- [103] Hah J, Nees J A, Hammig M D, Krushelnick K and Thomas A G R 2018 Characterization of a high repetition-rate laser-driven short-pulsed neutron source *Plasma Phys. Control. Fusion* **60** 054011
- [104] Tentori A 2018 *Laser-driven Neutron Sources: a First Numerical Investigation* Politecnico di Milano (<http://hdl.handle.net/10589/139122>)
- [105] Giovannelli A C 2019 *Medical Radioisotope Production by Means of Laser-driven Proton Accelerators: a Theoretical Study* Politecnico di Milano (<http://hdl.handle.net/10589/149404>)
- [106] Jung D *et al* 2013 Characterization of a novel, short pulse laser-driven neutron source *Phys. Plasmas* **20** 056706
- [107] Kleinschmidt A *et al* 2018 Intense, directed neutron beams from a laser-driven neutron source at PHELIX *Phys. Plasmas* **25** 053101
- [108] Storm M *et al* 2013 Fast neutron production from lithium converters and laser driven protons *Phys. Plasmas* **20** 053106
- [109] Bird J R, Williams J S and James S 1989 *Ion Beams for Materials Analysis* (Amsterdam: Elsevier)
- [110] Petibois C and Cestelli Guidi M 2008 Bioimaging of cells and tissues using accelerator-based sources *Anal. Bioanal. Chem.* **391** 1599–608
- [111] Karydas A G, Streeck C, Radovic I B, Kaufmann C, Rissom T, Beckhoff B, Jaksic M and Barradas N P 2015 Ion beam analysis of Cu(In,Ga)Se 2 thin film solar cells *Appl. Surf. Sci.* **356** 631–8
- [112] Macková A, MacGregor D, Azaiez F, Nyberg J and Piasetzky E 2016 *Nuclear Physics for Cultural Heritage* (Mulhouse, France: European Physical Society)
- [113] Šmit Ž and Holc M 2004 Differential PIXE measurements of thin metal layers *Nucl. Instruments Methods Phys. Res. Sect. B Beam Interact. with Mater. Atoms* **219–220** 524–9
- [114] Šmit Ž, Uršič M, Pelicon P, Trček-Pečak T, Šeme B, Smrekar A, Langus I, Nemeč I and Kavkler K 2008 Concentration profiles in paint layers studied by differential PIXE *Nucl. Instruments Methods Phys. Res. Sect. B Beam Interact. with Mater. Atoms* **266** 2047–59
- [115] Pandola L, Andenna C and Caccia B 2015 Validation of the Geant4 simulation of bremsstrahlung from thick targets below 3 MeV *Nucl. Instruments Methods Phys. Res. Sect. B Beam Interact. with Mater. Atoms* **350** 41–8
- [116] Metzkes J, Cowan T E, Karsch L, Kraft S D, Pawelke J, Richter C, Richter T, Zeil K and Schramm U 2011 Preparation of laser-accelerated proton beams for radiobiological applications *Nucl. Instrum. Methods Phys. Res., Sect. A* **653** 172–5
- [117] Raschke S, Spickermann S, Toncian T, Swantusch M, Boeker J, Giesen U, Iliakis G, Willi O and Boege F 2016 Ultra-short laser-accelerated proton pulses have similar DNA-damaging effectiveness but produce less immediate nitroxidative stress than conventional proton beams *Sci. Rep.* **6** 32441
- [118] Schollmeier M *et al* 2008 Controlled transport and focusing of laser-accelerated protons with miniature magnetic devices *Phys. Rev. Lett.* **101** 055004